Experimentally Accessible Measurement of Irreversibility in Stochastic Systems by Categorizing Single-Molecule Displacements

Alvaro Lanza,[1] Inés Martínez-Martín,[1] Rafael Tapia-Rojo,[1,2] and Stefano Bo[1,2]
[1]*Department of Physics, King's College London, London WC2R 2LS, United Kingdom*
[2]*Centre for the Physical Sciences of Life, King's College London, London WC2R 2LS, United Kingdom*

(Received 2 December 2025; accepted 14 July 2026; published 26 August 2026)

Quantifying the irreversibility and dissipation of nonequilibrium processes is crucial to understanding their behavior, assessing their possible capabilities, and characterizing their efficiency. We introduce a physical quantity that quantifies the irreversibility of stochastic Langevin systems from the observation of individual molecules' displacements. Categorizing these displacements into a few groups based on their initial and final positions allows us to measure irreversibility precisely without the need to know the forces and magnitude of the fluctuations acting on the system. For short times, our model-free estimate of irreversibility is related to entropy production by a conditional fluctuation theorem. For short times and, in general, for stationary protocols, our estimate provides a lower bound to the average entropy production. We validate the method on single-molecule force spectroscopy experiments of proteins subject to force ramps. We show that irreversibility is sensitive to detailed features of the energy landscape underlying the protein folding dynamics and suggest how our methods can be employed to unveil key properties of protein folding processes.

DOI: 10.1103/j3jk-k315 Subject Areas: Biological Physics, Statistical Physics

I. INTRODUCTION

Life is out of equilibrium, sustained by the supply of energy, which is dissipated in irreversible processes. Such energy supplies lift the strict constraints imposed by equilibrium and allow life to exhibit its astonishing variety. The further from equilibrium a system is driven, the richer its behavior can be, with strong fluxes, large irreversibility [1,2], enhanced sensing [3–8], better polymer copying [9–13], faster and more accurate reactions to the environment, and many other biologically relevant features [14,15]. To properly characterize a system, it is fundamental to assess how far from equilibrium it operates. This allows us to compare the costs (in terms of dissipation, irreversibility, and energy expenditures) to the benefits (in terms of enhanced performances) and quantitatively assess trade-offs [3,16,17]. Recent fundamental results, such as the thermodynamic uncertainty relation (TUR), have contributed to this analysis, unveiling that dissipation bounds precision [18], fluctuations [19], coherence, and correlations of these systems [20–22].

Modern single-particle tracking techniques allow us to probe the dynamics of a wide range of systems at small scales [23–29], revealing a fluctuating world. Such stochastic thermal fluctuations make it challenging to detect if the system is out of equilibrium and to quantify how far. Stochastic thermodynamics has provided a solid theoretical framework to define and quantify irreversibility and entropy in stochastic systems, revealing the laws governing their statistics, such as fluctuation theorems [1,2,30–33]. Applying this framework to experiments with limited information on the forces at play is far from trivial and has led to the development of many methods for measuring irreversibility in Markovian stochastic processes [16,34–52]. Many such methods rely on the thermodynamic uncertainty relation, which provides a lower bound to the entropy that is produced to achieve a certain accuracy [18,19,36,37,53] and requires only the mean and variance of observable currents. A recent work independent of the TUR obtained a bound to entropy in systems with time-dependent driving, using only these first two moments and the diffusion coefficient [45]. Machine-learning techniques [38,41] and related methods [39,42] have also been developed and also estimators from coarse-graining experimentally inaccessible degrees of freedom of full trajectories [34,40,44,54–56]. Despite this remarkable progress, applications to experimental systems remain challenging and, therefore, limited. While each method has its capabilities and constraints, the main roadblocks include obtaining sufficient data, knowledge of the forces acting on the system, and applicability to cases with time-dependent protocols.

Aiming for experimental applicability, we present a technique to calculate the irreversibility of Langevin systems based on the measurement of particles' displacements at finite time intervals, which are experimentally accessible in subcellular systems. The key insight behind the method is to compensate for the finite temporal resolution by categorizing the observed displacements into classes, which depend on their starting and final positions. The method requires no knowledge of the forces acting on the system or the diffusion coefficient, and we show it to provide a lower bound to entropy production for stationary systems or when the system can be observed with a high time resolution. For systems that can be measured at high frequency, the method also captures the space-dependent profile of local dissipation.

To validate the method, we perform single-molecule magnetic tweezers experiments on the mechanosensing protein talin, which we unfold and refold out of equilibrium using force ramps. By comparing wild-type (WT) and mutant protein domains with simulations, we show how quantifying irreversibility unveils subtle properties of the protein free-energy landscape.

We start the paper by briefly introducing the basic concepts of stochastic thermodynamics in Sec. II. In Sec. III, we introduce our method, which we apply to various case studies in Sec. IV. We close by discussing the results in Secs. V and VI.

II. STOCHASTIC THERMODYNAMICS OF LANGEVIN SYSTEMS

We consider systems described by the overdamped Langevin equation

$$\dot{x}_t = \frac{F}{\gamma} + \sqrt{2D}\xi_t, \tag{1}$$

where x_t is the degree of freedom we are tracking (for example, the position of a single particle), F is the deterministic force acting on it (which can depend on position and time), ξ_t is a Gaussian white noise satisfying $\langle \xi_t \xi_{t'} \rangle = \delta(t - t')$, and the fluctuation-dissipation theorem links the diffusion D to friction γ via the temperature T, $D = k_B T/\gamma$. The entropy produced along a trajectory $\mathbf{x}$ can be defined in terms of its irreversibility as the log-ratio

$$\Delta S_{\mathrm{tot}}(\mathbf{x}) \equiv k_B \ln \frac{\mathcal{P}(\mathbf{x})}{\mathcal{P}^R(\tilde{\mathbf{x}})}, \tag{2}$$

where $\mathcal{P}(\mathbf{x})$ is the probability of observing the trajectory $\mathbf{x}$ forward in time and $\mathcal{P}^R(\tilde{\mathbf{x}})$ is the probability of observing the time-reversed one [33]. Since the space of trajectories grows exponentially with their length, it is practically impossible to sample it efficiently, and nontrivial coarse-graining procedures are required [54,57–59]. Taking the average of Eq. (2) shows that the average entropy production can be written as a Kullback-Leibler divergence (D_{KL}):

$$\langle \Delta S_{\mathrm{tot}} \rangle = k_B D_{\mathrm{KL}}(\mathcal{P}(\mathbf{x}) || \mathcal{P}^R(\tilde{\mathbf{x}})), \tag{3}$$

where the D_{KL} for two probability distributions p and p' is defined as $D_{\mathrm{KL}}(p||p') \equiv \int dx p \ln(p/p')$. This expression agrees with the second law of thermodynamics, since Kullback-Leibler divergences are never negative. A key result of stochastic thermodynamics is that this definition of entropy coincides with the thermodynamic entropy defined by studying heat exchanges with reservoirs:

$$\Delta S_{\mathrm{tot}}(\mathbf{x}) = \underbrace{k_B \ln \frac{P_0(x_0)}{P_t(x_t)}}_{\Delta S_{\mathrm{sys}}} + \underbrace{\frac{1}{T}\int F(x_t) \circ dx_t}_{\Delta S_{\mathrm{env}}}, \tag{4}$$

which has contributions ΔS_{sys} due to changes in the entropy of the system and ΔS_{env} from dissipation into the environment. The average rate of entropy production can be written as [33] $\langle \dot{S}_{\mathrm{tot}} \rangle = \int dx \dot{\sigma}(x)$, where

$$\dot{\sigma}(x) \equiv k_B \frac{\nu^2(x)}{D} P(x), \tag{5}$$

with $\nu(x)$ the local mean velocity, related to the probability flux as $\nu(x) = j(x)/P(x)$. $\dot{\sigma}(x)$ corresponds to the average rate at which entropy is generated conditioned on being at position x times the probability density of being there.

III. MEASURING IRREVERSIBILITY

A. Classes of displacements and their distributions

We consider a system that is observed at discrete time intervals Δt, in which it moves from the initial position $x' \equiv x_t$ to $x \equiv x_{t+\Delta t}$, and define the displacement $\ell = x - x'$. We start by considering the case of stationary systems so that there is no dependence on the overall time t. We discuss the generalization to time-dependent dynamics in Sec. III C 2.

In many systems, such as biomolecular condensates [60], protein and DNA (un)folding [61,62], cell membrane domains [63], and broader diffusion in the cytoplasm [64], the diffusive motion takes place in physically distinct environments. For such heterogeneous diffusion, be it with respect to an inhomogeneous diffusion coefficient and/or complex energy landscapes, it is natural to group displacements on the basis of where they take place, which is a key novelty of our approach. We categorize displacements based on where the initial and final positions are with respect to reference boundaries. These displacement distributions were studied experimentally in Ref. [65] and shown to contain relevant information about the diffusive nature of motion in biomolecular condensates and their equilibrium properties [66]. In the example depicted in

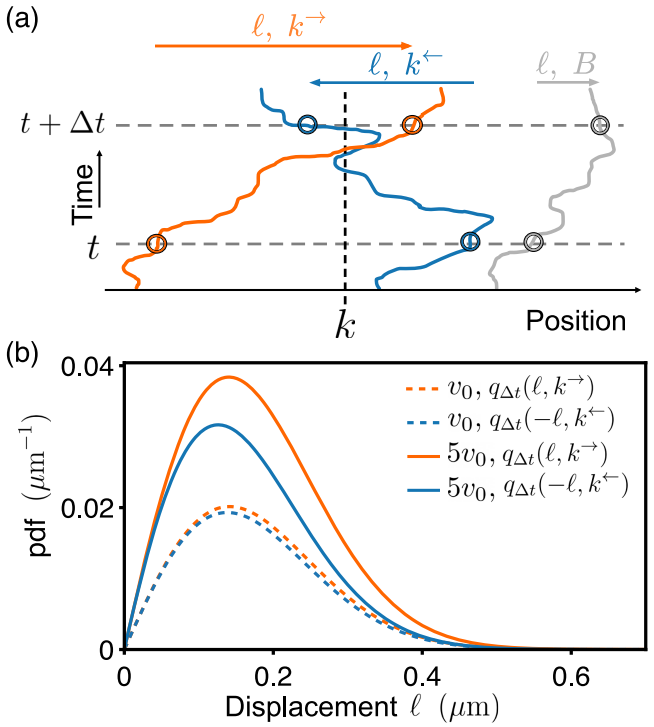

FIG. 1. (a) Illustration of displacements ℓ of three trajectories in the time window Δt, categorized into displacement classes with respect to the boundary at k. Trajectories of class $k^{\rightarrow}$ cross k left to right, $k^{\leftarrow}$ right to left, and B remain on the same side. (b) Probability density function (pdf) for displacements defined with respect to the boundary at $k = 0$ for the square potential on a ring [shown in Fig. 2(a)], at different driving speeds with $v_0 = 0.5\ \mu\text{m}\,\text{s}^{-1}$. At equilibrium, $q(\ell, k^{\rightarrow}) = q(-\ell, k^{\leftarrow})$.

Fig. 1(a), we draw a boundary at $x = k$ and partition all possible displacements into three classes, forming the set $\mathcal{C}_3 = \{k^{\rightarrow}, k^{\leftarrow}, B\}$. The last class is composed of displacements where the initial and final points are on the same side of the boundary (bulk, B), like the gray trajectory in Fig. 1(a). The remaining two classes are for displacements where the initial and final points are on opposite sides of k, where $k^{\rightarrow}$ and $k^{\leftarrow}$ denote displacements that cross k from left to right and right to left [orange and blue trajectories in Fig. 1(a), respectively]. Let us consider as an example, class $k^{\rightarrow}$, where $x' < k$ and $x > k$. The statistics of such displacements are described by the joint probability density of observing a displacement ℓ and of the displacement belonging to class $k^{\rightarrow}$:

$$q_{\Delta t}(\ell, k^{\rightarrow}) \equiv \int_{-\infty}^{k} dx' \int_{k}^{\infty} dx \delta(\ell - (x - x')) P_{\Delta t}(x|x') P(x'), \tag{6}$$

where $P(x')$ is the probability of finding the particle at x', $P_{\Delta t}(x|x')$ is the propagator, i.e., the probability of finding the particle in position x after a time Δt, given that it started at x', and δ denotes the Dirac delta function. We also define the marginal probability of observing a displacement of class $k^{\rightarrow}$:

$$p_{\Delta t}(k^{\rightarrow}) \equiv \int_{-\infty}^{k} dx' \int_{k}^{\infty} dx P_{\Delta t}(x|x') P(x'). \tag{7}$$

For a generic class of displacements C, the probability density is defined as

$$q_{\Delta t}(\ell, C) \equiv \iint_{\Omega_C} dx' dx \delta(\ell - (x - x')) P_{\Delta t}(x|x') P(x'), \tag{8}$$

where the integral is over the domain Ω_C, which defines the class, and

$$p_{\Delta t}(C) \equiv \iint_{\Omega_C} dx' dx P_{\Delta t}(x|x') P(x'). \tag{9}$$

By normalization, we have that $\sum_{C \in \mathcal{C}} \int d\ell\, q_{\Delta t}(\ell, C) = \sum_{C \in \mathcal{C}} p_{\Delta t}(C) = 1$.

B. Displacements and irreversibility

Displacements and their classes contain information about time reversibility. For example, for stationary systems, the time reversal of a displacement ℓ of class $k^{\rightarrow}$ is a displacement $-\ell$ of class $k^{\leftarrow}$ (and vice versa), while time reversal of bulk displacements still belongs to the same class. In general, we denote by $\tilde{C}$ the class associated with the time reversal of a displacement of class C. Formally, they are found by exchanging initial and final positions, x' and x. For the example in Fig. 1(a), the time-reversed classes of $k^{\rightarrow}$, $k^{\leftarrow}$, and B correspond to $k^{\leftarrow}$, $k^{\rightarrow}$, and B, respectively. For a general partition, including n classes of displacements, $\mathcal{C}_n$, we define the following measure of irreversibility:

$$\Sigma_{\Delta t}(\mathcal{C}_n) \equiv k_B \sum_{C \in \mathcal{C}_n} \int d\ell\, q_{\Delta t}(\ell, C) \ln \frac{q_{\Delta t}(\ell, C)}{q_{\Delta t}(-\ell, \tilde{C})}, \tag{10}$$

which is the Kullback-Leibler divergence of the mixed (discrete in C, continuous in ℓ) joint probabilities between time-forward and reversed displacements over all classes and is the key contribution of this work. This measure of irreversibility is based on coarser measurements that focus on the initial and final points x' and x in a displacement taking a time Δt and ignore the intermediate positions visited by the paths. Therefore, it is easier to estimate from experimental data than the full path probabilities with Eq. (3).

C. Irreversibility and entropy

At equilibrium, the detailed balance condition $P_{\Delta t}(x|x')P(x') = P_{\Delta t}(x'|x)P(x)$ ensures that $q_{\Delta t}(\ell, C) = q_{\Delta t}(-\ell, \tilde{C})$, resulting in $\Sigma_{\Delta t} = 0$, as seen, for a special case, in Ref. [66]. This suggests a relation between the coarse measure of irreversibility $\Sigma_{\Delta t}$ and entropy production defined in Eq. (2), which we explore in this section.

In the limit of vanishing Δt, entropy production can be expressed in terms of the breaking of the detailed balance condition, and Eq. (2) can be written as

$$\lim_{\Delta t\to 0} \Delta S_{\mathrm{tot}}(x|x') = k_B \lim_{\Delta t\to 0} \ln \frac{P_{\Delta t}(x|x')P(x')}{P_{\Delta t}(x'|x)P(x)}, \quad (11)$$

where $\Delta S_{\mathrm{tot}}(x|x')$ denotes the entropy produced in a trajectory starting at position x' and arriving at position x. As shown in Appendix B, for small Δt, by exchanging the initial and final points x' and x, the probability distribution of a displacement $q_{\Delta t}(\ell, C)$ can be expressed in terms of the same integrals appearing in the definition of the time-reversed displacement $q_{\Delta t}(-\ell, \tilde{C})$, weighted by the exponential of the entropy produced in the displacement. One can then obtain that the ratio of the displacement distribution, and its time reversal obeys the conditional fluctuation theorem

$$\lim_{\Delta t\to 0} \frac{q_{\Delta t}(-\ell, \tilde{C})}{q_{\Delta t}(\ell, C)} = \lim_{\Delta t\to 0} \langle e^{-\Delta S_{\mathrm{tot}}/k_B} | \ell, C\rangle, \quad (12)$$

where the right-hand side is the conditional average of the exponential of minus the entropy that is produced in a displacement, provided that this displacement is ℓ and of class C. For a one-dimensional stationary system, this holds for all Δt, as shown in Sec. I in Supplemental Material [67] and in a similar result [83] based on splitting probabilities. A more general fluctuation theorem of this kind was obtained in Ref. [84] by considering a broader definition of classes, not defined only in terms of the initial and final points. Equation (3) expresses the average entropy production in terms of a Kullback-Leibler divergence of the path probabilities. From an information-theoretic viewpoint, this implies that if instead of observing the full trajectories in detail, we have access to only coarse-grained measurements, we will typically obtain a lower bound to the entropy production [54,57]. This is a consequence of the fact that projecting or marginalizing two distributions cannot increase their Kullback-Leibler divergence, which is known as the data-processing inequality and proven by the log-sum inequality [85]. [For non-negative a_i and b_i, the log-sum inequality states $\sum a_i \log(a_i/b_i) \geq a \log(a/b)$, where $a = \sum_i a_i$ and $b = \sum_i b_i$.] The displacements we are considering record the initial and final points (x' and x, respectively) but ignore the intermediate points visited in the time interval Δt. This projection, combined with Eq. (3), provides a lower bound to entropy production $\langle \Delta S_{\mathrm{tot}}\rangle \geq k_B D_{\mathrm{KL}}(P_{\Delta t}(x', x)||P_{\Delta t}(x, x'))$. This bound is saturated for one-dimensional stationary processes or for generic processes in the small Δt limit (see Sec. I in Supplemental Material [67]). Furthermore, the displacements retain only $\ell = x - x'$ and the type of displacement (i.e., less information than x and x'). Because of this coarse-graining, comparing the displacements to their time reversal provides the lower bound

$$\Sigma_{\Delta t}(\mathcal{C}_n) \leq \langle \Delta S_{\mathrm{tot}}\rangle \quad \text{(steady state)}, \quad (13)$$

as shown explicitly in Appendix A. We remark that this bound holds for stationary dynamics and discuss the time-dependent case in Sec. III C 2.

1. A hierarchy of bounds

Intuitively, categorizing the displacements in many different classes has the potential of achieving a tighter bound to entropy production. This intuition can be made precise by the data-processing inequality. Let us consider a partition including n classes $\mathcal{C}_n$. If two of these classes are merged, we obtain a partition with $n - 1$ classes, which we call $\mathcal{C}'_{n-1}$. (Note that this merging procedure is not unique, and different classes $\mathcal{C}'_{n-1}$ exist.) We can repeat the procedure until we are left with a single class, including all the possible displacements, which we denote as $\mathcal{I}$, for which the time reversal simply corresponds to flipping the sign of ℓ. For these partitions, we have the hierarchy of bounds

$$0 \leq \Sigma_{\Delta t}(\mathcal{I}) \leq \cdots \leq \Sigma_{\Delta t}(\mathcal{C}'_{n-1}) \leq \Sigma_{\Delta t}(\mathcal{C}_n) \leq \langle \Delta S_{\mathrm{tot}}\rangle. \quad (14)$$

2. Time-dependent dynamics

For time-dependent dynamics, the probabilities of observing displacements evolve in time. It is then necessary to generalize our approach to take into account the time t when the displacements are observed and consider the time-dependent displacement probability distribution $q_{\Delta t,t}(\ell, C)$, with the added time in the subscript t denoting the starting time of the displacement. To assess irreversibility, we compare displacements starting at time $t - \Delta t$ and ending at t to displacements starting at time t and ending at time $t + \Delta t$. This guarantees that the starting time of the reversed displacements corresponds to the ending time of the forward displacement, as detailed in Appendix A 1. Our definition of irreversibility, then, generalizes to the time-dependent case as

$$\Sigma_{\Delta t,t}(\mathcal{C}_n) \equiv k_B \sum_{C\in\mathcal{C}_n} \int d\ell\, q_{\Delta t,t-\Delta t}(\ell, C) \ln \frac{q_{\Delta t,t-\Delta t}(\ell, C)}{q_{\Delta t,t}(-\ell, \tilde{C})}. \quad (15)$$

Systems where the applied forces do not vary in time relax toward a steady state. For such relaxation dynamics, $\Sigma_{\Delta t,t}$

provides a lower bound to the average entropy produced in the $[t-\Delta t, t]$ time window $\langle \Delta S_{\mathrm{tot}} \rangle_{t-\Delta t}^{t}$:

$$\Sigma_{\Delta t,t}(\mathcal{C}_n) \leq \langle \Delta S_{\mathrm{tot}} \rangle_{t-\Delta t}^{t} \quad \text{(relaxation)}. \tag{16}$$

If the applied forces follow a time-dependent protocol, Eq. (15) still provides a well-defined measure of irreversibility. However, this measure provides a lower bound to the average entropy production only in the limit of a short time window $\Delta t \to 0$, for which the time reversal of the protocol plays a negligible role (see Appendix A 1 b):

$$\lim_{\Delta t \to 0} \Sigma_{\Delta t,t}(\mathcal{C}_n) \leq \langle \Delta S_{\mathrm{tot}} \rangle_{t-\Delta t}^{t} \quad \text{(time-dep driving)}. \tag{17}$$

D. Local dissipation

Let us now focus on the case where we have a single boundary at k as in Fig. 1(a). Disregarding the length of the displacements, the probability of a displacement crossing the boundary [defined in Eq. (7)] provides an alternative measurement of irreversibility. For a steady state, it reads

$$\Sigma_{\Delta t}^{\mathrm{trans}}(k) \equiv k_B [p_{\Delta t}(k^{\rightarrow}) - p_{\Delta t}(k^{\leftarrow})] \ln \frac{p_{\Delta t}(k^{\rightarrow})}{p_{\Delta t}(k^{\leftarrow})}, \tag{18}$$

while the definition for the time-dependent case is discussed in Appendix A 1. Since it disregards the length of the displacements, this measure is coarser compared to the one defined in Eq. (10). As a consequence, it is easier to estimate from experimental data, but it captures less irreversibility, since $\Sigma_{\Delta t}^{\mathrm{trans}}(k) \leq \Sigma_{\Delta t}(\mathcal{C}_3)$. In the limit of short time intervals Δt, $\Sigma_{\Delta t}^{\mathrm{trans}}$ provides an estimate of the dissipation locally occurring around k. Defining the diffusive length scale $\ell_0 = \sqrt{\pi D \Delta t}$, we have (see Sec. II in Supplemental Material [67] for the derivation)

$$\frac{\Sigma_{\Delta t}^{\mathrm{trans}}(k)}{\Delta t} = \ell_0 \dot{\sigma}(k) + \mathcal{O}(\Delta t^{3/2}), \tag{19}$$

where the density of dissipation rate $\dot{\sigma}(x)$ is defined in Eq. (5).

IV. CASE STUDIES

A. Nonequilibrium steady states

1. Driven particle on a ring

As a first example, we consider a particle on a ring subject to a constant force $F = v\gamma$. The system reaches a nonequilibrium steady state with a constant (in time and space) probability distribution and a constant probability flux $j \propto v$. This leads to a constant entropy production rate [see Eq. (5)], and in a time Δt, there is an average entropy production $\langle \Delta S_{\mathrm{tot}} \rangle = k_B v^2 \Delta t / D$. The displacement distributions can be calculated analytically, because the propagators are Gaussian and the steady-state distribution is space independent. Since the system is uniform in space, it is not necessary to partition the displacements, and $\Sigma_{\Delta t}(\mathcal{I}) = k_B v^2 \Delta t / D$ coincides with total entropy produced, with $\Sigma_{\Delta t}(\mathcal{I}) = \Sigma_{\Delta t}(\mathcal{C}) \ \forall \ \mathcal{C}$. For this example, a suitably defined TUR bound [see Eq. (20)] and methods based on milestoning [83,86] and other coarse-grainings [40,57] also capture the full dissipation.

2. Driven particle in a square potential on a ring

As a second, richer example, we consider a particle on a ring inside a square potential well, as shown in Fig. 2(a). The well extends from $x = -L$ to $x = 0$ and has height ΔW: $W(x) = \Delta W[\Theta(x) + \Theta(-x - L)]$, where $\Theta(x) = 1$ for $x > 0$ and 0 otherwise. We implement the ring by imposing periodic boundary conditions at $x = -L$ and $x = L$. In addition to the potential, the particle is subject to a constant nonconservative force γv so that in Eq. (1) $F = -\nabla W + \gamma v$. This force creates a nonequilibrium steady state and pushes the particle on one side of the well, accumulating a peak in probability distribution which decays exponentially within the well (over a length D/v) and exhibits a sharp drop upon leaving the well. We report the probability distributions for different amounts of driving v in Fig. 2(b) and give the explicit expressions in Sec. III in Supplemental Material [67]. For larger external forces, the peak within the well becomes narrower and the profile away from the peak becomes flatter [compare the blue and red curves in Fig. 2(b)]. The propagators for this model can be computed analytically [87], and integrating them provides explicit expressions for the displacement distributions, which we report in Sec. III in Supplemental Material [67] and illustrate in Fig. 1(b) for $q(\ell, k^{\rightarrow})$ and $q(-\ell, k^{\leftarrow})$ at $k = 0$. As expected, the difference between a displacement and its time reverse increases as the system is driven further from equilibrium. To obtain $\Sigma_{\Delta t}$, we integrate these displacement distributions numerically. In this example, since the system is not homogeneous in space, considering more classes of displacements refines the estimated irreversibility. We compare three ways of partitioning the possible displacements: a single class, $\mathcal{I}$, the three classes defined with respect to the crossing of a boundary at $x = k_1$, $\mathcal{C}_3(k_1) = \{k_1^{\rightarrow}, k_1^{\leftarrow}, B\}$, and a more refined partition that considers a second boundary at $x = k_2$, with six classes of displacements $\mathcal{C}_6(k_1, k_2) = \{k_1^{\rightarrow}, k_1^{\leftarrow}, B_L, B_R, k_2^{\rightarrow}, k_2^{\leftarrow}\}$, as illustrated in Fig. 2(a). (We consider timescales such that displacements crossing both boundaries have negligible probabilities, i.e., $k_2 \pm k_1 \gg \sqrt{D\Delta t}$, $k_2 \pm k_1 \gg v\Delta t$.) As predicted by the hierarchy of bounds Eq. (14), considering more classes of displacements allows us to greatly improve the estimate, capturing more irreversibility, as shown in Figs. 2(d) and 2(e). How much irreversibility each estimator captures depends on how far from equilibrium the system is driven [see Fig. 2(d)] and on where we place the boundary k_1 [see Fig. 2(e)]. The first

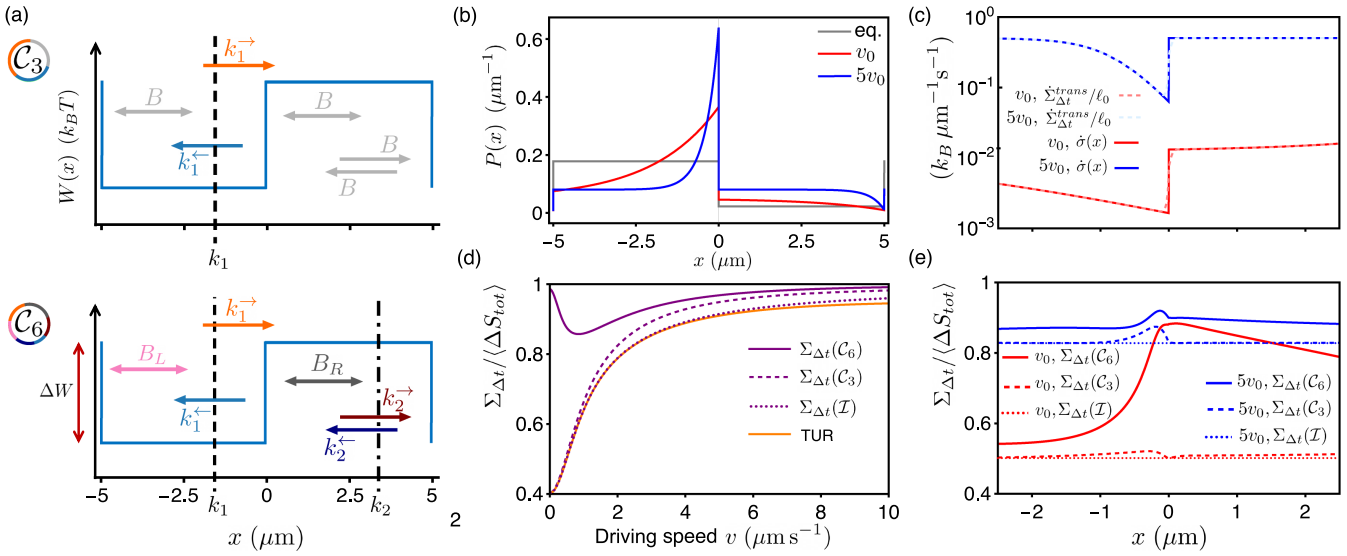

FIG. 2. (a) Profile of square potential $W(x)$ and different classes of displacements: (top) $\mathcal{C}_3(k_1)$ and (bottom) $\mathcal{C}_6(k_1, k_2)$. (b) Steady-state probability distributions for a particle in a square potential on a periodic topology, subject to different constant drivings v with $v_0 = 0.5\ \mu\text{m s}^{-1}$. For the equilibrium (eq.) distribution, $v = 0$. (c) Local dissipation: the solid lines give the density of entropy production rate $\dot{\sigma}$ defined in Eq. (5) for near ($v = 0.5$) and far ($v = 2.5$) from equilibrium driving. The dashed curves are the local irreversibility estimates obtained from $\dot{\Sigma}^{\text{trans}}_{\Delta t} = \Sigma^{\text{trans}}_{\Delta t}/\Delta t$ [see Eqs. (18) and (19)], as a function of the position of the boundary $k_1 = x$. (d) Fraction of irreversibility captured ($\Sigma_{\Delta t}/\langle \Delta S_{\text{tot}} \rangle$) for three types of displacement partitions $\mathcal{I}$ (purple dotted line), $\mathcal{C}_3(k_1 = -0.1)$ (purple dashed line), $\mathcal{C}_6(k_1 = -0.1, k_2 = \pm 5)$ (purple solid line), and TUR (orange line) as a function of the nonequilibrium driving v. (e) $\Sigma_{\Delta t}/\langle \Delta S_{\text{tot}} \rangle$ for different partitions as a function of the boundary location k_1 for far and near equilibrium driving (blue and red lines, respectively), with $k_2 = \pm 5$ fixed. For all drivings considered in the plots above, $D = 1\ \mu\text{m}^2\ \text{s}^{-1}$, $\gamma = 1 k_B T\ \text{s}\,\mu\text{m}^{-2}$, $\Delta W = k_B T \ln 8$, and irreversibilities are measured with $\Delta t = 10$ ms.

interesting finding is that, when we do not distinguish between classes of displacements, $\Sigma_{\Delta t}(\mathcal{I})$ tracks closely the dissipation measured via the TUR. Figure 2(d) shows how the estimators approach one another and the average entropy production as the system is driven further from equilibrium. This is likely due to the fact that the system becomes "more homogeneous" (more similar to the case without the potential) as the driving increases, making it less important to distinguish different classes of displacements. For systems near equilibrium, distinguishing the displacements can greatly improve the irreversibility estimate. Interestingly, $\Sigma_{\Delta t}(\mathcal{C}_6(k_1, k_2))$ displays a nonmonotonic dependence on the external driving, capturing accurately the dissipation as $v \to 0$. A reason for this is that the homogeneity of the system is also nonmonotonic with v. For instance, the steady-state probability depicted in Fig. 2(b) shows how, away from the boundary, the profile is flat at equilibrium (gray curve), displaying a marked gradient at intermediate driving (red curve) and approaching flatness again for higher driving (blue curve). Far from equilibrium, the plateaus inside and outside the potential are at the same value (blue curve), while at equilibrium they are at different levels (gray curve). This suggests that, near equilibrium, it may be advantageous to consider separately the displacements taking place inside or outside the well. This is achieved by the partition $\mathcal{C}_6$ with the boundaries located near the potential barriers $k_1 \simeq 0$, $k_2 \simeq L$. To gather further insight, in Fig. 2(e), we show the fraction of the average entropy production $\langle \Delta S_{\text{tot}} \rangle$ that is captured by $\Sigma_{\Delta t}$, as a function of where we set the boundary k_1 (k_2 is kept at $x = L$). As a reference, not grouping displacements into separate classes, $\Sigma_{\Delta t}(\mathcal{I})$ captures only 50% of $\langle \Delta S_{\text{tot}} \rangle$ near equilibrium ($v = 0.5\,\mu\text{m s}^{-1}$) and up to 83% further from equilibrium ($v = 2.5\ \mu\text{m s}^{-1}$). As anticipated, adding a boundary at $x = k_1$ provides an improvement when the boundary is drawn in the vicinity of the potential barrier that the force is pushing toward, $k \simeq 0$. Further away, the improvement is slight. $\Sigma_{\Delta t}(\mathcal{C}_6(k_1, k_2))$ provides a significant increase, especially for the near-equilibrium case, where placing a boundary at $k_1 \simeq 0$ nearly doubles the amount of dissipation captured. There is also a stronger dependence on where the boundary is drawn. The main contribution to the increase comes from splitting the two bulk classes B_R and B_L, where the displacements are markedly different (indeed, the probability of crossing a boundary scales with $\sqrt{\Delta t}$, so for the short times we are considering, there are relatively few crossings, so that crossing displacements in classes $\{k_1^{\rightarrow}, k_1^{\leftarrow}, k_2^{\rightarrow}, k_2^{\leftarrow}\}$ play a minor role). In Fig. S1 in Supplemental Material [67], we plot the six displacement distributions of $\Sigma^{(6)}_{\Delta t}(\mathcal{C}_6)$ for the near- and far-from-equilibrium cases at their optimal k_1.

Note that, for a particle on a one-dimensional ring, it is possible to recover the full entropy production using

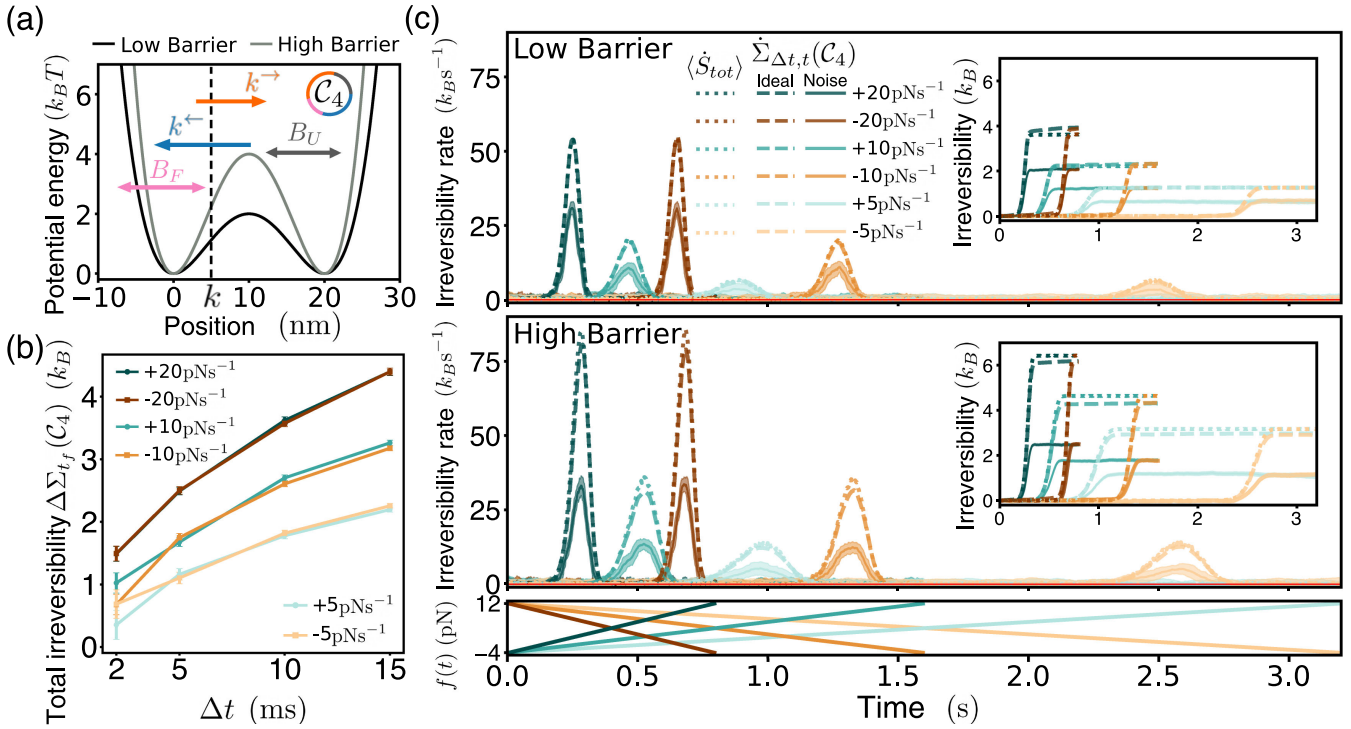

FIG. 3. (a) Symmetric double-well potential with a high ($\Delta U = 4k_BT$) and low ($\Delta U = 2k_BT$) barrier and $x_M = L = 10$ nm. Arrows indicate the types of displacements measured in the $\mathcal{C}_4$ classification used to calculate $\Sigma_{\Delta t,t}(\mathcal{C}_4)$. The boundary used to define the displacements is located at k. (b) Influence of displacement time Δt on the total measured irreversibility $\Delta\Sigma_{t_f}(\mathcal{C}_4)$ in each force ramp, for the high barrier case with measurement noise. (c) Entropy production rate $\langle\dot{S}_{\rm tot}\rangle$ (dotted lines), computed via Eq. (4), and irreversibility rate $\dot{\Sigma}_{\Delta t,t}$ for different pulling rates for low and high potential barriers, respectively. Solid curves: running average of the irreversibility rate estimate $\dot{\Sigma}_{\Delta t,t}(\mathcal{C}_4)$, measured every millisecond with $\Delta t = 5$ ms, using 5000 trajectories and adding measurement noise. The running averages are taken over 70, 35, and 18 points for the $|r| = 5$, 10, and 20 curves, respectively, while the shaded error regions are taken from the running standard deviation over the same windows. Dashed curves: $\dot{\Sigma}_{\Delta t,t}(\mathcal{C}_4)$ but estimated from 50 000 trajectories without measurement noise. Inset: cumulative time integral of measured irreversibility $\Delta\Sigma_t(\mathcal{C}_4)$ and entropy $\langle\Delta S_{\rm tot}\rangle$. Bottom: trace of pulling force curves with time, for the different ramp rates as color-coded above. $k_BT = 4.11$ pN nm and $D = 3000$ nm^2 s^{-1}.

discrete transition statistics [46,47,83], which can be obtained through the coarse-graining procedure known as milestoning [86]. In an empirical setting, the data requirements of this procedure are different from $\Sigma_{\Delta t}(\mathcal{C}_6)$. Depending on the situation, $\Sigma_{\Delta t}(\mathcal{C}_6)$ can return more accurate estimates of entropy production as we illustrate in Sec. V in Supplemental Material [67] with simulated data for the settings described in Fig. 2, discussed in Sec. V B 1.

Figure 2(c) shows that the local dissipation can be estimated accurately with Eq. (19), counting displacements crossing a boundary located at k_1 via $\Sigma^{\rm trans}_{\Delta t}(k_1)$ for times up to $\Delta t = 10$ ms, which corresponds to a length scale $\ell_0 = 0.18$ μm.

B. Double-well potential under force ramps

After discussing stationary cases, we now consider a scenario subject to a time-dependent driving. In this case, the time-dependent irreversibility $\Sigma_{\Delta t,t}$ as defined in Eq. (15) provides a bound to entropy production only in the vanishing Δt limit [Eq. (17)]. In this section, we show that highly informative measurements of irreversibility can be obtained despite this limitation.

We consider a particle in a symmetric double-well potential $W(x) = \Delta U[(x - x_M)^2/L^2 - 1]^2$, where x_M is the location of the potential barrier, which is of height ΔU. L is the distance between the maximum and either of the two minima. Double-well potentials are ubiquitous as a model of bistability in physics and have been successfully employed to model protein and RNA (un)folding [88], chemical reactions [89], etc. In anticipation of our experimental analysis of the thermodynamics of proteins under force ramps in Sec. IV C, we tilt the potential by an external time-dependent force $f(t) = f_0 + rt$ linearly with rate r, so that the force in Eq. (1) is $F(x,t) = -\nabla W(x) + f(t)$. We consider two potentials, characterized by relatively low and high barrier heights as sketched in Fig. 3(a), with parameters also motivated by the experimental regime. For initial and final forces $f_0 = -4$ pN and $f_{\rm f} = 12$ pN, we explore three different pulling rates r: 5, 10, and 20 pN s^{-1}, where the total duration of each experiment is $t_f = (f_{\rm f} - f_0)/r$.

We also look at the opposite protocol, with $f_0 = 12$ pN and $f_f = -4$ pN and the same but negative rates. Trajectories are always initialized from the equilibrium distribution at a tilt of f_0. To estimate irreversibility in this scenario, we identify four types of displacements by placing the measurement boundary k between the two wells $\mathcal{C}_4 = \{k^{\rightarrow}, k^{\leftarrow}, B_F, B_U\}$ as in Fig. 3(a), where $k^{\rightarrow}$ and $k^{\leftarrow}$ displacements represent crossing from the left to the right well (unfolding for a protein model) and vice versa (folding for a protein model). Class B_F (B_U) includes displacements that stay in the left (right) well, representing fluctuations in the folded (unfolded) state. In agreement with the hierarchy of bounds [Eq. (14)], we found this $\mathcal{C}_4$ classification captures more irreversibility than the $\mathcal{C}_3$ with one bulk term, as shown in Sec. VI in Supplemental Material [67]. We fix k throughout each ramp (one can potentially vary it at each measurement time) but place it at different locations for each of the six ramp types we explore, choosing the location that records the most irreversibility in total. We show how $\Sigma_{\Delta t}$ depends on the location of k in Sec. XII in Supplemental Material [67]. The dashed lines in Fig. 3(c) show the numerical evaluation of the dissipation rate $\dot{\Sigma}_{\Delta t,t}(\mathcal{C}_4) = \Sigma_{\Delta t,t}(\mathcal{C}_4)/\Delta t$, which tracks closely the average total entropy production $\langle \Delta S_{\mathrm{tot}} \rangle$ reported as the dotted lines (for the low barrier case, the lines are barely distinguishable). The peaks of the dissipation estimate (and of the entropy production rate) correspond to the occurrence of transitions across wells, as they agree with the transition probability curves shown in Sec. VI in Supplemental Material [67]. This differs from the nonequilibrium steady-state case studied above, as the crossing $(k^{\rightarrow}, k^{\leftarrow})$ terms are now main contributors to $\Sigma_{\Delta t}(\mathcal{C}_4)$. The locations of these peaks in time are different between the unfolding (positive r) and refolding (negative r) ramps, despite the potential well being symmetric. This is simply because the protocols start at forces that are not equidistant with respect to the coexistence force of $f = 0$. As expected, faster ramps are more irreversible and accompanied by higher dissipation, visible in the height of the peaks in Fig. 3(c) and in the total irreversibility $\Delta\Sigma_t = \int_0^t dt' \dot{\Sigma}_{\Delta t,t'}$ shown in the insets (we measure every millisecond so $dt' = 1$ ms). We also see that barrier hopping is more reversible for the potential with the lower barrier, as testified both by entropy production and by our measure of irreversibility.

In an experiment, only a finite number of ramps can be recorded, which complicates the empirical estimation of the Kullback-Leibler divergences. This is not a trivial task for continuous distributions of small datasets [46,90], as simply "plugging in" binned probabilities to the base D_{KL} formula raises systematic biases and is strongly dependent on the chosen binning. In Sec. IV in Supplemental Material [67], we discuss our implementation of the nearest-neighbor algorithm for a continuous probability D_{KL} [91] to the case of the mixed discrete-continuous $\Sigma_{\Delta t}(\mathcal{C}_n)$. To test the robustness of our method, we consider the case of 5000 ramps simulated via Brownian dynamics. We additionally explore the effect of measurement noise by adding to the recorded simulated positions a Gaussian noise with variance 9 nm^2. This value is motivated by the instrumental noise of our magnetic tweezer setup (see Sec. XIV in Supplemental Material [67]). The resulting curves are shown as full lines in Fig. 3(c) and indicate that the empirical measure still captures very well the location of the dissipation peaks. The height and the width of the peaks are smaller because measurement noise influences in the same way the forward and the time-reversed displacements, making their distribution more similar. However, the rescaling is consistent across conditions, testifying that our method can be used to compare irreversibility in different conditions for experimentally relevant settings. The error shading from our estimator in Fig. 3(c) denotes the running standard deviation. In Sec. IV 1 in Supplemental Material [67], we show that the addition of noise is the principal factor responsible for the rescaling, while the reduction of the sample size plays a minor role.

In Fig. 3(b), we explore how varying the time over which we compute irreversibility affects the estimate on simulated data, using this noisy dataset. We see that larger Δt gives rise to higher dissipation estimates but that the overall ranking that sees faster ramps dissipating more and both positive and negative ramps dissipating similarly is conserved among different times (i.e., the lines corresponding to different ramp rates do not cross). This suggests that the estimated irreversibility yields robust information under varying extents of nonequilibrium drivings and that it can be used to systematically compare which system is more dissipative. The dependence on Δt, however, suggests keeping the same Δt when comparing different scenarios. (What influences the estimate is how Δt compares with the timescales of the system, one of which is set by the pulling rate, another by the typical oscillation timescales near the potential bottom, and another one by the transition rates across the barrier. This suggests caution when comparing widely different systems.) Large Δt can provide irreversibility estimates that exceed entropy production, as already evident by the noiseless estimate at $r = \pm 20$ pN s^{-1} in the low barrier inset in Fig. 3(c). We choose $\Delta t = 5$ ms in an effort to balance the trade-off between the advantage of larger time steps, which provide a sufficient number of transitions across k, and the requirement of short time steps to closely monitor dissipation. For this, the time steps should be much shorter than the typical timescales of the system, which include the timescales of the protocol, the intrawell relaxation times, and the unfolding and refolding ones.

C. Experimental protein unfolding and refolding under force ramps

To test our measure of irreversibility on an experimental two-state system, we use single-molecule magnetic tweezers on a mechanosensitive protein. We study the nonequilibrium protein unfolding and refolding dynamics upon

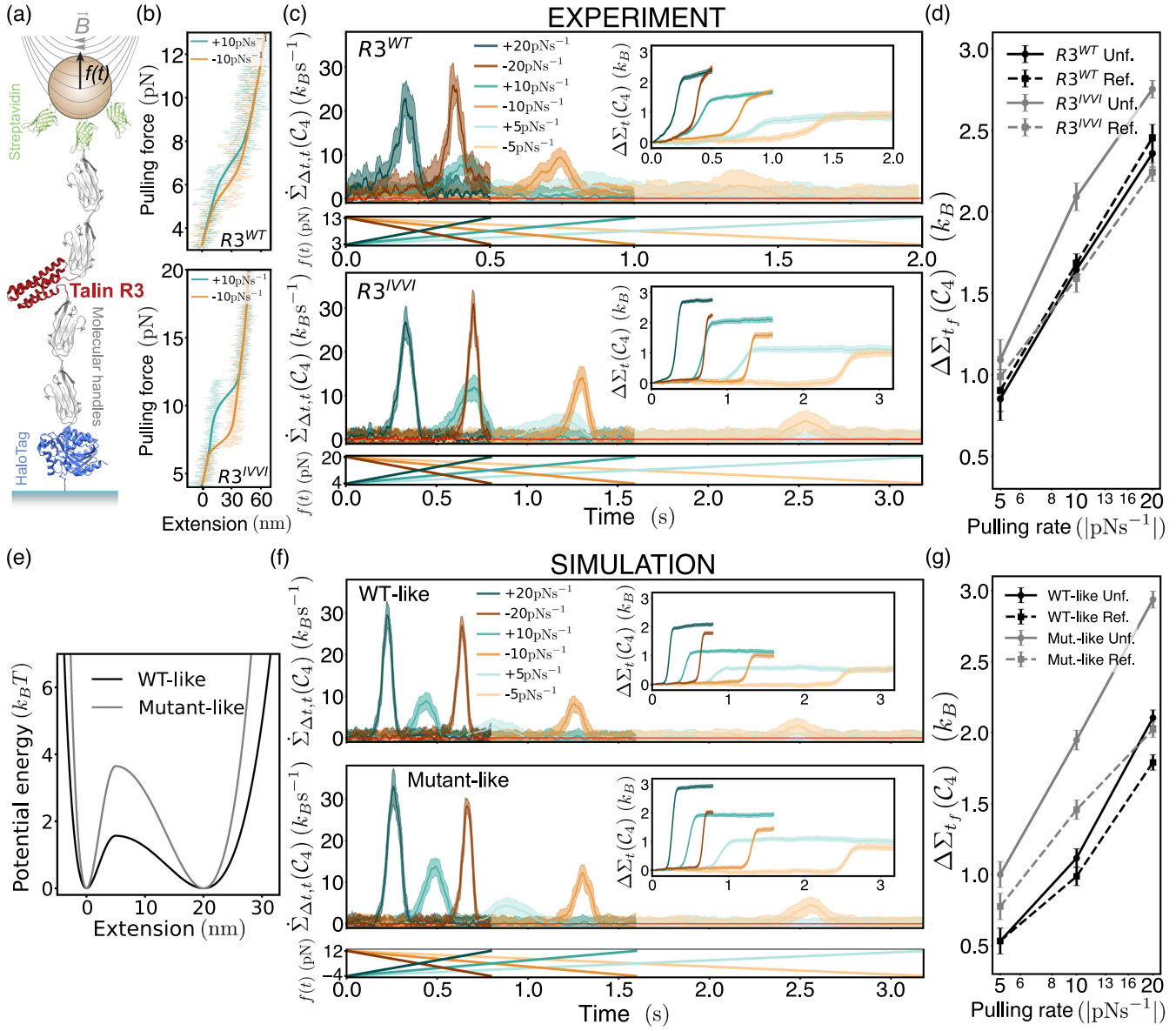

FIG. 4. (a) Schematic of experimental magnetic tweezer setup. (b) Thin traces: example trajectories of the talin R3 extension as the pulling force is linearly increased (blue) and decreased (orange) at $r = \pm 10$ pN s^{-1}, for the wild-type R3$^{\mathrm{WT}}$ (top) and mutant R3$^{\mathrm{IVVI}}$ (bottom). The thick curves show the respective mean extension over all of the experiments. (c) Irreversibility rate $\dot{\Sigma}_{\Delta t,t}(\mathcal{C}_4)$ measurements from experiments on the R3$^{\mathrm{WT}}$ (top) and mutant R3$^{\mathrm{IVVI}}$ (bottom) protein domains at different pulling rates. Measuring every millisecond with $\Delta t = 5$ ms, we show the running average over 70, 35, and 18 points for the $|r| = 5$, 10, and 20 curves, respectively. Inset: cumulative time integral $\Delta\Sigma_t(\mathcal{C}_4)$ of measured irreversibility. Lower: pulling forces for each ramp rate as color coded above. (d) Total irreversibility at the end of each protocol as a function of unfolding (positive) and refolding (negative) pulling rates. The shown data are obtained from 1682, 5000, and 1441 trajectories for $|r| = 5$, 10, and 20 on the R3$^{\mathrm{WT}}$ and 3933, 3500, and 5322 on the R3$^{\mathrm{IVVI}}$, respectively. (e) Simulations are performed on the shown asymmetric potentials, with $D = 3000$ nm^2 s^{-1}, $k_BT = 4.11$ pN nm. The potential with the lower energy barrier mimics the wild-type (WT) R3$^{\mathrm{WT}}$ protein and the high barrier the mutant R3$^{\mathrm{IVVI}}$ construct. (f) As in (c) for 5000 simulated trajectories for the wild-type-like, low-barrier potential (WT-like), and mutant-like, high-barrier potential, with added noise on the recorded positions. (g) As in (d) for the simulated data.

cyclic linear force ramp protocols, using the setup presented in Ref. [28] and shown in Fig. 4(a). As a model protein system, we choose talin R3, a force-sensing protein domain at focal adhesions showcasing a low mechanical stability, unfolding at forces of just approximately 5 pN. Engineered mutations in its four-threonine belt residue (R3$^{\mathrm{IVVI}}$) increase its mechanical stability to approximately 9 pN while keeping its physiological function intact [92,93]. Both the R3 wild-type R3$^{\mathrm{WT}}$ and the R3$^{\mathrm{IVVI}}$ mutant have been previously characterized as classic

two-state folders whose native folding dynamics under force are well described by a one-dimensional double-well energy landscape along the end-to-end pulling coordinate, similar to Fig. 3(a) [28,94]. [Over long timescales ($\sim 10^4$ s), $R3^{IVVI}$ has been shown to populate reversible misfolded states, therefore departing from the simple two-state folding scenario. However, these dynamics are not relevant to the fast nonequilibrium experiments of this work.] We confirm this by conducting constant force experiments and using the committor and transition path tests for one-dimensional diffusion [88,95], as shown in Sec. VII in Supplemental Material [67]. The results indicate that, indeed, protein extension is a suitable projection of the protein dynamics, following a one-dimensional diffusion in a bistable landscape. Our measure of irreversibility and the alternative ones we discuss in Sec. V are based on this one-dimensional diffusive description. As usual, dissipation in faster, unobservable degrees of freedom cannot be excluded [96,97].

As magnetic tweezers enable direct control of the pulling force, we subject a single $R3^{WT/IVVI}$ domain to a nonequilibrium pulling force protocol. As in the simulations in Sec. IV B, we increase the force linearly between two values f_0 and f_f for a time t_f. We make sure that the protein is equilibrated in the folded state at f_0 ($f_0 = 3$ pN for $R3^{WT}$ and $f_0 = 4$ pN for $R3^{IVVI}$) before starting the ramp. Once the unfolding ramp is completed, we keep the force constant to allow the protein to relax and in the unfolded state at f_f ($f_f = 13$ pN for $R3^{WT}$ and $f_f = 20$ pN for $R3^{IVVI}$). We then perform the refolding ramp, linearly decreasing the force back to f_0. The high stability of magnetic tweezers enables us to probe the (un)folding dynamics of a single protein by cycling this force protocol thousands of times (see Fig. S22 [67] for the protocol and some examples of the recorded trajectories). Additionally, and in order to modulate the degree of irreversibility in our experiment, we probe three different pulling rates for each protein, $r = \pm 5$, ± 10, and ± 20 pN s^{-1}. The dynamics of the system upon a force cycle are characterized by force-extension traces as shown in Fig. 4(b), displaying the typical hysteresis loops between the unfolding (green) and refolding (orange) force ramps due to the nonequilibrium nature of the system (see Fig. S9 [67] for force-extension curves at other pulling rates). The area enclosed in the loop represents the total work dissipated in an unfolding and refolding cycle. As expected, the average dissipated work increases with the pulling rate, and the $R3^{WT}$ protein shows lower dissipation than $R3^{IVVI}$, likely due to its lower mechanical stability.

To compute the irreversibility over the nonequilibrium unfolding and refolding ramps, we identify the same four classes of displacements $\mathcal{C}_4$ as discussed for the simulations [Fig. 3(a)] and compute $\Sigma_{\Delta t,t}(\mathcal{C}_4)$ as per Eq. (15) using the estimator discussed in Sec. IV in Supplemental Material [67]. The magnetic tweezers setup allows for a measurement frame rate of approximately 1 ms^{-1}, so we calculate $\Sigma_{\Delta t,t}(\mathcal{C}_4)$ every 1 ms, and, as in the simulations, the accumulated dissipation is calculated as $\Delta\Sigma_t = \int_0^t dt' \dot{\Sigma}_{\Delta t,t'}$ with $dt' = 1$ ms. Guided by the simulation results in Sec. IV B [Fig. 3(b)], we choose $\Delta t = 5$ ms for all the ramps. In Fig. S12 [67], we show how different choices of Δt influence the irreversibility estimation in experiments. The hysteresis loops in Fig. 4(b) show that unfolding and refolding events occur stochastically at different forces, which leads to different extension changes following the polymer elasticity of an unfolded protein. We therefore choose to place the boundary k at different locations for the unfolding and refolding ramps, as discussed in Sec. XII in Supplemental Material [67]. For instance, at $r = \pm 10$ pN s^{-1} we find the best choice of displacement partitions $k = 24$ and 19 nm for the unfolding and refolding ramps of $R3^{IVVI}$, respectively. For the wild-type domain, we place them at $k = 30$ and 28 nm.

As in the simulated scenarios, the peaks of irreversibility [Fig. 4(c)] take place when most unfolding and refolding events occur, shown by the survival probabilities in Fig. S11 [67]. As a second finding, we confirm the expected trend that faster ramps are more irreversible, as manifested by larger total irreversibility $\Delta\Sigma_{t_f}$ in Fig. 4(d). For the wild type, unfolding and refolding ramps are similarly irreversible as in the simulations in Sec. IV B. Surprisingly, for the $R3^{IVVI}$ mutant, unfolding is systematically more irreversible than refolding. The lower panel in Fig. 4(c) shows that this difference is due to the peaks of irreversibility being broader for the unfolding events (mostly visible for the $r = 10$ pN s^{-1} pulling rate). This effect is not predicted by the symmetric simulations in Sec. IV B, therefore calling for the development of a richer model to describe the folding dynamics of talin R3.

Previous analytical studies based on simplified free-energy landscapes obeying Bell-Evans kinetics and experiments on DNA hairpins have highlighted that the distance between each of the wells and the barrier governs the irreversibility of the folding and unfolding processes [98]. We, therefore, hypothesize that the difference we observe may also be linked to asymmetries in the free-energy landscape. Evidence from long equilibrium experiments conducted close to the coexistence force suggests an asymmetric folding landscape, where the unfolded well is broader than the folded one and, thus, further from the barrier [94]. This hypothesis is further supported by the different force sensitivity in the folding and unfolding rates (Fig. S8 [67]). We, therefore, set out to test whether an asymmetric potential with a narrower folded well recapitulates the experimental observation that unfolding is more irreversible than refolding, by performing numerical simulations.

We choose the asymmetric potential wells to be $W(x) = \Delta U[(a(x - x_M)/L)^2 - 1]^2$, where the asymmetry factor $a = 1$ for $x < L$ and $a = 1/3$ for $x \geq L$. Since the

mutant is more mechanically stable, we model it with a higher potential barrier ($\Delta U = 3.65 k_B T$) compared to the wild type ($\Delta U = 1.56 k_B T$), as shown in Fig. 4(e) and discussed in Sec. VIII in Supplemental Material [67]. The simulations in an asymmetric potential show that unfolding is more irreversible than refolding for the high-barrier (mutant-like) potential, while this difference vanishes for the low-barrier (wild-type-like) case, as reported in Fig. 4(g). This recapitulates the experimental observation. Furthermore, Fig. 4(f) shows that the difference in irreversibility for the mutant-like simulations stems from the wider peaks in the irreversibility profile of the unfolding ramps, as observed experimentally. Figures 4(d) and 4(g) show that, for the low-barrier (wild-type-like) potential, the irreversibility is very similar for unfolding and refolding, as seen in the experiments. The simulations also confirm the qualitative trend that (as for the symmetric case) the peaks of irreversibility of the mutant are higher than those of the wild type. The difference in the total irreversibility is more pronounced in the simulations than in the experiments [Figs. 4(d) and 4(g)], mostly owing to the wild-type experiment featuring some dissipation also away from the folding and refolding transitions [see $\Delta\Sigma_t$ gradients at start and end of protocols in the top in Fig. 4(c), inset]. These gradients are not due to early or late folding or unfolding events, which are very rare for these times, as can be seen in the survival probability shown in Fig. S11 [67]. This is confirmed by the fact that the main contribution to irreversibility is given by displacements in the class associated with the folded and unfolded states. This irreversibility may arise from the nonequilibrium stretching of the polymer.

V. DISCUSSION

A. Summary of the results

We have introduced an experimentally accessible, model-free, direct measure of irreversibility based on classifying displacements according to their location and comparing them with suitably defined time-reversal displacements. The method is experimentally feasible, because it does not attempt to sample the overwhelmingly large space of trajectories and focuses on the initial and final points of displacements. The risk of overlooking dissipation in this potentially lossy approach is mitigated by the fact that the method distinguishes displacements that take place in different locations. We have discussed the relation between the irreversibility estimated by our method and entropy production, to which it can provide a lower bound for stationary dynamics, for systems relaxing toward a steady state, and, in general, in the short-time limit. By studying a forced particle in a potential on a ring, we have shown how the method captures more irreversibility than a naive TUR and progressively improves as we increase the number of classes in which we categorize the displacement. We have also shown how, by monitoring the system at relatively high (but experimentally feasible) frequency, the method can identify the spatial profile of dissipation, as shown in Fig. 2(c). We have showcased the method's potential in time-dependent nonequilibrium systems and demonstrated how it can be applied to study single-molecule force-spectroscopy experiments. This demonstrates that the applicability of the method is not restricted to ideal situations but extends to experiments where measurement noise and a limited number of trajectories impact the study.

B. Relation to existing measures of irreversibility

A direct comparison between the measure of irreversibility we are presenting and existing methods in the literature is not straightforward. The main difficulty lies in the scarcity of model-free methods that can be applied to time-dependent continuous systems (such as driven Langevin systems) without requiring nontrivial processing of the data. This is easier for stationary systems, where the TUR can be directly applied, as we discuss below. For time-dependent systems, however, this is challenging. Applications of the TUR to systems under time-dependent force protocols require observing the response of the system to slight changes in the driving at every time point [37] or knowledge of the spatial derivatives of the full force [49] (and, thus, an error-free estimation of the energy landscape).

An alternative approach to characterize irreversibility involves slicing the time-dependent trajectory into short intervals and applying the TUR on each of the intervals. The machine-learning method of Ref. [41] and the estimator of Ref. [42] optimize this approach and show accurate applicability to an RNA unfolding protocol. These methods come at the cost of decreasing interpretability and require nontrivial hyperparameter and architecture optimization. We discuss the performances of Ref. [41] and of a short-time displacements TUR on our experimental data in Sec. V B 2 and Sec. XIII 2 in Supplemental Material [67].

In addition, the recent method presented in Ref. [44] is suitable for studying linear force ramps of a protein, but it requires both the forward and backward protocols. Additionally, it needs sampling of two continuous random variables, the times of starting and completing (un)folding transitions in both protocols, which are binned in two dimensions, which makes it rather data intensive. We present its implementation for our experimental data in Sec. XIII 3 in Supplemental Material [67] and summarize its performance in Sec. V B 2.

The method of Ref. [45] is accessible and not data intensive but requires knowing the diffusion coefficient. This is challenging to estimate for systems evolving in the complex energy landscapes (such as proteins) measured at finite time resolution [99] and made additionally difficult

by measurement noise [100]. In Sec. XIII 1 in Supplemental Material [67], we compare our method to that of Ref. [45] for simulations in which D is known *a priori*. We find that, while the trend of higher dissipation at higher driving is also inferred, our method better captures the relative difference in irreversibility between low and high barrier systems and between folding and refolding ramps, as shown in Fig. S16 [67]. For the experimental studies, due to the challenges in measuring the diffusion coefficient, we assume a reference space constant diffusion coefficient in both protein constructs. This prevents us from comparing the magnitude of the estimators but allows us to study their profiles in time and trends across experimental conditions. While the trends are roughly consistent, the method of Ref. [45] does not capture that unfolding is more irreversible than folding in the $R3^{IVVI}$ construct at any pulling rate.

1. Relation to the TUR and milestoning for stationary systems

For stationary systems, it is possible to directly compare our method to estimates made by the TUR using the same type of displacement statistics. The TUR provides a lower bound to entropy production by considering the mean and fluctuations of a time-integrated current. The displacements we are considering can be analyzed with a TUR approach since ℓ is an integrated current over the time window Δt, $\ell = \int_{t=0}^{t=\Delta t} dx_t$ satisfying the $\ell \to -\ell$ odd-parity under time reversal. For such a current, the TUR gives a bound of the entropy production by the mean net displacement $\langle \ell \rangle$ and its variance as

$$2k_B \frac{\langle \ell \rangle^2}{\langle \ell^2 \rangle - \langle \ell \rangle^2} \leq \langle \Delta S_{\mathrm{tot}} \rangle. \tag{20}$$

This type of analysis does not take advantage of categorizing the displacements based on where they take place. In this respect, it can be compared to our method for the partitioning where all displacements belong to the same class $\mathcal{I}$. Our case studies confirm that the two measures yield similar estimates of irreversibility, as shown in Fig. 2(d). For the cases we considered, categorizing displacements based on where they occur returns a better estimate of irreversibility, making them preferable to the TUR, especially for cases where the dynamics vary considerably in space. When the system is driven far from equilibrium, all estimators capture more of the irreversibility (as noted for the TUR in a sinusoidal potential in Ref. [48]), but our method still outperforms the TUR. It would be an interesting future direction to investigate the relation between the multidimensional TUR and our method based on categorizing displacements [42].

We also compare the estimate provided by $\Sigma_{\Delta t}(\mathcal{C}_6)$ to that of the milestoning method of Ref. [86] on simulated data from the nonequilibrium steady state in a potential illustrated in Fig. 2, as detailed in Sec. V in Supplemental Material [67]. For a particle on a one-dimensional ring, milestoning is known to recover the full entropy production rate for long trajectories sampled at short time intervals. However, for finite trajectory length and time intervals, $\Sigma_{\Delta t}(\mathcal{C}_6)$ can capture a higher fraction of entropy production, and milestoning may also overestimate entropy production. The comparison in Fig. S4 [67] shows that, far from equilibrium, $\Sigma_{\Delta t}(\mathcal{C}_6)$ provides a more reliable estimate of entropy production for a finite amount of data, with faster convergence. Increasing the number of milestones provides a faster convergence but, due to the finite sampling time Δt, results in an overestimation of the entropy production for longer trajectories as shown in Fig. S5 [67]. Closer to equilibrium, milestoning converges faster than $\Sigma_{\Delta t}(\mathcal{C}_6)$ but is still prone to overestimations. Increasing the sampling time Δt improves the convergence of $\Sigma_{\Delta t}(\mathcal{C}_6)$ and makes the overestimation of milestoning more severe. These results suggest the advantage of using our method for short trajectories far from equilibrium and for trajectories that cannot be sampled at high frequency.

2. Comparison of methods to estimate dissipation in protein pulling experiments

Our method does not involve the difficult exponential average of Jarzynski-like estimators, which are typically biased [101,102], and is more robust to the presence of outliers. Additionally, unlike estimators using Crooks' relation [32], it does not require performing experiments with both the time-forward and time-backward protocols. However, since our experimental protocol contains both the forward and backward protocols, we are able to estimate the dissipated work using Crooks' relation and cross-validate our results. The dissipated work computed via Crooks' relation is directly linked to entropy production when the protocol starts and ends at equilibrium. The trend that wild-type talin R3 is more reversible than the IVVI mutant is confirmed, as is the fact that, for the mutant, unfolding is more irreversible than refolding. We report these measurements in Figs. S20 and S21 [67].

We stress that, for systems driven by time-dependent protocols, $\Sigma_{\Delta t,t}$ is a lower bound to entropy production only for vanishing Δt. However, the presence of measurement noise decreases the irreversibility estimated by $\Sigma_{\Delta t,t}$ and typically mitigates the risk of overestimating entropy production, as shown in Figs. 3 and S13 [67]. One should, anyway, recall that the exact value of $\Delta\Sigma_t$ depends on the chosen Δt, as shown in Figs. 3(b) and S12 [67]. As a consequence, the relative amount of irreversibility captured by the method can depend on the magnitude of Δt relative to the relevant timescales. In the experiments we performed, for $\Delta t = 5$ ms, we estimate the fraction relative to the dissipated work to be in the range between 14 and 36%, as shown in Fig. S21(b) [67], where the higher values are obtained for faster pulling rates and the wild type, which are

characterized by faster dynamics (resulting in relatively larger Δt). Nonetheless, $\Delta\Sigma_t$ provides a principled and systematic measurement of irreversibility, as confirmed by the high degree of correlation with the dissipated work measured by Crooks' relation shown in Fig. S21(a) [67].

Having access to both the forward and reverse protocols allows us to implement the method in Ref. [44]. We find that, while the estimates of the wild type are fairly robust, the results for the IVVI mutant are crucially sensitive to the specific implementation of the method, depending strongly on how the discrete states are chosen and the histogram binning (see Fig. S19 [67]). As suggested in Ref. [44], when data are limited, it is advisable to bin the histogram coarsely. We find that, with this choice and a suitable selection of the states (which is nontrivial without knowing the ground truth), the correct irreversibility trends can be identified [see Fig. S19(d) [67]].

Similarly to our approach, one could use other estimates devised for stationary or short-time dynamics and apply them to time-dependent systems measured over small time intervals. We compare our experimental estimates of irreversibility $\Sigma_{\Delta t,t}$, to the TUR taken at short-time displacements, and the machine-learning technique [41] for time-dependent entropy production. This is more extensively discussed in Sec. XIII 2 in Supplemental Material [67]. Both techniques produce similar results to $\Sigma_{\Delta t,t}$ on the wild type but do not recover all the expected trends in the more irreversible mutant, as shown in Fig. S17 [67]. For instance, the method in Ref. [41] with the default architecture and hyperparameter choice does not reproduce the increase of dissipation with higher pulling rates, finding a higher dissipation for the intermediate ramp at 10 pN/s than for the fast one at 20 pN/s. Furthermore, both alternative methods typically find a lower dissipation for the mutant than for the wild type, which is in contrast with the results from $\Sigma_{\Delta t,t}$, and Crooks' relation. The short-time TUR also erroneously predicts that unfolding dissipates less than refolding. The estimates of $\Sigma_{\Delta t,t}$ are in line with physical expectations (faster ramps dissipate more), with numerical simulations (higher irreversibility for unfolding and for more stable proteins), and confirmed by independent estimates via Crooks' relation. The discrepancies of the short-time TUR and the methods from Refs. [41,45] suggest $\Sigma_{\Delta t,t}$ is more reliable at estimating irreversibility in these experiments.

C. Applications to biomolecular folding

Stochastic thermodynamics and its application to biomolecular folding have a rich history, dating back to Jarzynski and Crooks' seminal work [31,32]. The application of fluctuation theorems to nonequilibrium single-molecule rupture experiments has enabled the recovery of folding free energies, in general, with good agreement with bulk biochemical data [103] and, more recently, of other thermodynamic quantities such as enthalpy or heat capacity changes [104]. These methodologies require starting from an equilibrium case and, therefore, have mostly been employed to study thermodynamic differences between the folded and unfolded states. Our measurement of irreversibility naturally handles nonequilibrium scenarios, providing detailed profiles of how irreversibility evolves in time. This offers new insight into the molecular mechanisms that drive transitions between the folded and unfolded states.

By precisely quantifying irreversibility, we have demonstrated that it is possible to distinguish thermodynamic differences between the folding mechanisms of the R3 wild type and the widely studied $R3^{IVVI}$ mutant. Strikingly, while the mechanically fragile wild-type variant exhibits nearly symmetric unfolding and refolding transitions, $R3^{IVVI}$ shows higher irreversibility for unfolding compared to refolding. We traced back this asymmetry to features of the underlying energy landscape, in which the unfolding barrier lies closer to the folded basin, producing distinct curvatures for the folded and unfolded wells. These results agree with the observations made for DNA hairpins [98,105].

From the perspective of protein folding, talin R3 shows a rather unique behavior, hallmarked by its exquisite force sensitivity for both unfolding and refolding that underpins its biological function as a threshold for cellular mechanotransduction [106]. By contrast, most classically studied proteins are mechanically rigid, unfolding at high forces with only weak force dependence in their unfolding rates while refolding at very low forces. This large mechanical hysteresis generates a high dissipation during unfolding and refolding cycles, a property that could be essential to protect cellular structures against mechanical shocks [107]. In this context, we speculate that such shock-absorbing proteins will be characterized by more pronounced asymmetries in entropy production across cyclic force protocols. Applying our method to these proteins would allow us to disentangle the differences in dissipation between folding and unfolding, identifying which step is responsible for most of the dissipation.

VI. CONCLUSIONS

Investigating the out-of-equilibrium behavior of small systems sheds light on their features, properties, and capabilities. This is especially valuable for living systems, which typically operate away from equilibrium. To this aim, we have proposed an experimentally accessible model-free method and related it to entropy production. We have highlighted the situations where the relation with entropy is tight and scrutinized the reasons behind it. For stationary systems, the method can be leveraged to provide a spatial profile of dissipation identifying where the system dissipates the most. Testing the method on nonequilibrium force-spectroscopy measurements of proteins revealed how, by providing a quantitative framework

for nonequilibrium thermodynamics in biomolecular transitions, our method is sensitive to subtle mechanical and thermodynamic signatures that govern protein responses to force. This establishes it as a rigorous tool for rationalizing the function of mechanically active proteins.

The method we have proposed relies on the displacements measured at fixed time intervals. In the future, it will also be interesting to explore approaches where time is the random variable being observed to probe equilibrium, as done, for example, in Refs. [108–112].

ACKNOWLEDGMENTS

S. B. thanks Frank Jülicher for suggesting using the difference in displacement distributions to measure irreversibility. The authors also acknowledge inspiring and insightful discussions with Izaak Neri, Adarsh Raghu, Lennart Dabelow, Lars Hubatsch, Martina Bulgari, Tan Van Vu, and Felix Ritort. We thank Patricia Paracuellos for expression and purification of the protein constructs and Sergi Garcia-Manyes for use of the molecular biology equipment. R. T.-R. is supported by an Engineering and Physical Sciences Research Council (EPSRC) Horizon Europe Guarantee ERC Starting Grant (EP/Y036085/1), an EPSRC ECR International Collaboration Grant (EP/Y001125/1), and a Royal Society Research Grant (RG/R2/232147).

DATA AVAILABILITY

The data that support the findings of this article are not publicly available. The data are available from the authors upon reasonable request.

APPENDIX A: PROOF OF THE ENTROPY BOUND

To prove that our measure of irreversibility gives a lower bound to entropy production [Eq. (13)], we proceed in two steps. The first step is to show that considering only the initial and final points of a displacement contains less information about irreversibility than the whole trajectory. The second step demonstrates that focusing on displacements $\ell = x - x'$ and on which class they belong to instead of retaining both x' and x results in a further loss of information. We start by introducing the notation $P_{\Delta t}(x', x) = P_{\Delta t}(x|x')P(x')$ to denote the joint probability of starting with a particle in position x' and finding it in position x after a time Δt. Note that the order of the two variables matters, and $P_{\Delta t}(x, x') = P_{\Delta t}(x'|x)P(x)$ denotes the joint probability of starting in x and arriving at x'.

Starting from Eq. (3), we can marginalize the intermediate points in the trajectories $x' \to x$. For a Markov process, this yields the joint probabilities as a function of the propagator and the initial distribution $P_{\Delta t}(x', x) = P_{\Delta t}(x|x')P(x')$. Therefore, as shown in Sec. I in Supplemental Material [67],

$$D_{\mathrm{KL}}(\mathcal{P}(\mathbf{x})||\mathcal{P}(\tilde{\mathbf{x}})) \geq D_{\mathrm{KL}}(P_{\Delta t}(x', x)||P_{\Delta t}(x, x')), \tag{A1}$$

where equality holds for one-dimensional systems and for systems where the propagator obeys a detailed-balance-like condition $\log[P(x|x')/P(x'|x)] = g(x) - g(x')$ for a generic function g. For the second step, let us reexpress the Kullback-Leibler divergence as a sum over the different classes of displacements that we are considering. For a generic collection of classes $\mathcal{C}_n$, we have

$$D_{\mathrm{KL}}(P_{\Delta t}(x', x)||P_{\Delta t}(x, x')) = \sum_{C \in \mathcal{C}_n} \iint_{\Omega_C} dx' dx P_{\Delta t}(x', x) \ln \frac{P_{\Delta t}(x', x)}{P_{\Delta t}(x, x')}. \tag{A2}$$

Each class C is defined by its support in x' and x, Ω_C, meaning from which region the displacement starts in and in which region it arrives at. The time reversal of a displacement entails swapping the initial and final points. The time reversal of displacements belonging to class C, then, belong to class $\tilde{C}$ with a support over domain $\Omega_{\tilde{C}}$ where the initial and final domains are swapped (i.e., x' and x are exchanged). We restrict ourselves to the case in which the domains are continuous intervals such that they can be written as $x' \in [x'^C_{\min}, x'^C_{\max}]$ and $x \in [x^C_{\min}, x^C_{\max}]$, with $x'^C_{\min} < x'^C_{\max}$ and $x^C_{\min} < x^C_{\max}$. The integral over the domain Ω_C can then be written in terms of Heaviside theta functions, yielding

$$\iint_{\Omega_C} dx' dx = \int_{-\infty}^{\infty}\int_{-\infty}^{\infty} dx' dx [\Theta(x' - x'^C_{\min}) - \Theta(x' - x'^C_{\max})] \times [\Theta(x - x^C_{\min}) - \Theta(x - x^C_{\max})]. \tag{A3}$$

We define the short-hand notation

$$\theta^C_{x',x} \equiv [\Theta(x' - x'^C_{\min}) - \Theta(x' - x'^C_{\max})] \times [\Theta(x - x^C_{\min}) - \Theta(x - x^C_{\max})], \tag{A4}$$

substitute these into Eq. (A2), and perform the change of variables $x \to x' + \ell$ with $d\ell = dx$ to get

$$D_{\mathrm{KL}}(P_{\Delta t}(x', x)||P_{\Delta t}(x, x')) = \sum_{C \in \mathcal{C}_n} \int_{-\infty}^{\infty}\int_{-\infty}^{\infty} dx' d\ell \theta^C_{x',x'+\ell} P_{\Delta t}(x', x' + \ell) \times \ln \frac{P_{\Delta t}(x', x' + \ell)}{P_{\Delta t}(x' + \ell, x')}. \tag{A5}$$

Note $x^C_{\min}$ and $x^C_{\max}$ are constants, which remain in $\theta^C_{x',x'+\ell}$, which reads

$$\theta^C_{x',x'+\ell} = [\Theta(x' - x'^C_{\min}) - \Theta(x' - x'^C_{\max})][\Theta(x'+\ell - x^C_{\min}) - \Theta(x'+\ell - x^C_{\max})], \tag{A6}$$

thus enforcing the same domain after the change of variables.

Focusing on a single C term of the class summation above, we can introduce the theta terms in the log-ratio and apply the log-sum inequality for a dx' integration:

$$\begin{aligned}\int_{-\infty}^{\infty}\int_{-\infty}^{\infty} dx' d\ell\, \theta^C_{x',x'+\ell} P_{\Delta t}(x', x'+\ell) \ln \frac{\theta^C_{x',x'+\ell} P_{\Delta t}(x', x'+\ell)}{\theta^C_{x',x'+\ell} P_{\Delta t}(x'+\ell, x')} \\ \geq \int_{-\infty}^{\infty} d\ell \int_{-\infty}^{\infty} dx' \theta^C_{x',x'+\ell} P_{\Delta t}(x', x'+\ell) \ln \frac{\int_{-\infty}^{\infty} dx' \theta^C_{x',x'+\ell} P_{\Delta t}(x', x'+\ell)}{\int_{-\infty}^{\infty} dx' \theta^C_{x',x'+\ell} P_{\Delta t}(x'+\ell, x')},\end{aligned} \tag{A7}$$

where the inequality follows from the log-sum inequality, which states that, for non-negative a_i and b_i, $\sum a_i \log(a_i/b_i) \geq a \log(a/b)$, where $a = \sum_i a_i$ and $b = \sum_i b_i$. The integrands in x' on the rhs of Eq. (A7) can be linked to the displacement distributions. The term appearing in the numerator in the log-ratio coincides with the definition of the joint displacement distributions $q_{\Delta t}(\ell, C)$, as can be shown by carrying out the integral over x in Eq. (8):

$$q_{\Delta t}(\ell, C) \equiv \iint_{\Omega_C} dx' dx \delta(\ell - (x - x')) P_{\Delta t}(x|x') P(x') = \int_{-\infty}^{\infty} dx' \theta^C_{x',x'+\ell} P_{\Delta t}(x', x'+\ell). \tag{A8}$$

The denominator of the log-ratio of Eq. (A7) is the integral of the time reverse joint probability $P_{\Delta t}(x'+\ell, x') = P_{\Delta t}(x'|x'+\ell) P(x'+\ell)$ but still in the support $\theta^C_{x',x'+\ell}$ of the forward class C. To connect to Eq. (10), we wish to express this integral in terms of the displacements in the time-reverse class $\tilde{C}$. Since the domain of the time-reverse displacements $\tilde{C}$ corresponds to swapping the initial and final domains of the original class, we have $\theta^C_{x',x'+\ell} = \theta^{\tilde{C}}_{x'+\ell,x'}$ (as one can check by direct substitution). We then have (renaming the dummy integrating variable x' as x for convenience)

$$\begin{aligned}\int_{-\infty}^{\infty} dx \theta^C_{x,x+\ell} P_{\Delta t}(x+\ell, x) &= \int_{-\infty}^{\infty} dx \theta^{\tilde{C}}_{x+\ell,x} P_{\Delta t}(x+\ell, x) \\ &= \iint_{\Omega_{\tilde{C}}} dx' dx P_{\Delta t}(x|x') P(x') \delta(\ell - (x' - x)) = q_{\Delta t}(-\ell, \tilde{C}).\end{aligned} \tag{A9}$$

This shows how the rhs of Eq. (A7) simplifies as

$$\int_{-\infty}^{\infty} d\ell \int_{-\infty}^{\infty} dx' \theta^C_{x',x'+\ell} P_{\Delta t}(x', x'+\ell) \ln \frac{\int_{-\infty}^{\infty} dx' \theta^C_{x',x'+\ell} P_{\Delta t}(x', x'+\ell)}{\int_{-\infty}^{\infty} dx' \theta^C_{x',x'+\ell} P_{\Delta t}(x'+\ell, x')} = \int_{-\infty}^{\infty} d\ell\, q_{\Delta t}(\ell, C) \ln \frac{q_{\Delta t}(\ell, C)}{q_{\Delta t}(-\ell, \tilde{C})}. \tag{A10}$$

Recalling the definition of our measure of irreversibility from Eq. (10), the bound expressed in Eq. (13) then follows by applying the log-sum inequality Eq. (A7) to each class in $\mathcal{C}_n$. To summarize the proof and illustrate the bound, the two steps of information processing, starting from the full path probabilities, give

$$\begin{aligned}\langle \Delta S_{\text{tot}} \rangle &= k_B D_{\text{KL}}(\mathcal{P}(\mathbf{x}) || \mathcal{P}^R(\tilde{\mathbf{x}})) \\ &\geq k_B D_{\text{KL}}(P_{\Delta t}(x', x) || P_{\Delta t}(x, x')) \\ &\geq \Sigma_{\Delta t}(\mathcal{C}_n).\end{aligned} \tag{A11}$$

This bound holds for any stationary systems described by an overdamped Langevin process. In the following subsection, we explain how it is generalized to nonstationary cases where the underlying forces are not time dependent.

1. Time-dependent systems

We present here the generalization of our measure of irreversibility to time-dependent systems Eq. (15) and discuss its relation to entropy production. We consider two types of time-dependent systems: systems subject to a time-constant force profile, relaxing toward a steady state,

and systems that are driven by time-dependent force protocols. For time-constant profiles, we show how the measure of irreversibility provides a lower bound to entropy production for arbitrary Δt, while for time-dependent force protocols this holds in the $\Delta t \to 0$. We discuss the properties of the measure of irreversibility for finite Δt.

a. Relaxation dynamics

Consider the entropy production $\langle \Delta S_{\rm tot} \rangle^t_{t-\Delta t}$ in a time window Δt, happening between the times $t-\Delta t$ and t. When the forces governing the Langevin dynamics are time independent, but the system has not relaxed to a steady state yet, we have a time dependence in the joint probability due to the starting distribution $P_{\Delta t,t-\Delta t}(x',x) = P_{\Delta t}(x|x')P_{t-\Delta t}(x')$. In analogy to what we showed for time-independent dynamics in Eq. (A1), we have

$$\begin{aligned}\langle \Delta S_{\rm tot} \rangle^t_{t-\Delta t} &\geq k_B D_{\rm KL}(P_{\Delta t,t-\Delta t}(x',x)||P_{\Delta t,t}(x,x')) \\ &= k_B \iint dx'dx P_{\Delta t}(x|x')P_{t-\Delta t}(x') \\ &\quad \times \ln \frac{P_{\Delta t}(x|x')P_{t-\Delta t}(x')}{P_{\Delta t}(x'|x)P_t(x)}. \end{aligned} \tag{A12}$$

The main difference with Eq. (A2) is that for the time reversal the trajectories start at time t, and the position is distributed according to $P_t(x)$. We take this into account for classifying the displacements where the joint probability $q_{\Delta t,t-\Delta t}(\ell, C)$ of displacements $\ell = x_t - x'_{t-\Delta t}$ starting at $t-\Delta t$ in class C and $q_{\Delta t,t}(-\ell, \tilde{C})$ for the time-reverse displacements $-\ell = x_t - x'_{t+\Delta t}$ in class $\tilde{C}$. With this identification, we generalize our measure of irreversibility to time-dependent systems by defining

$$\Sigma_{\Delta t,t}(\mathcal{C}_n) \equiv k_B \sum_{C\in\mathcal{C}_n} \int d\ell\, q_{\Delta t,t-\Delta t}(\ell, C) \ln \frac{q_{\Delta t,t-\Delta t}(\ell, C)}{q_{\Delta t,t}(-\ell, \tilde{C})}. \tag{A13}$$

This is Eq. (15) in the main text. Following the same logic as for the time-independent case discussed above, this quantity provides a lower bound to the average entropy production

$$\langle \Delta S_{\rm tot} \rangle^t_{t-\Delta t} \geq \Sigma_{\Delta t,t}(\mathcal{C}_n). \tag{A14}$$

An additional remark is necessary for the calculation of $\Sigma^{\rm trans}_{\Delta t}$ under transience, modifying its definition Eq. (18). The marginal probabilities of belonging to class C defined in Eq. (9) now have a global time t component

$$\begin{aligned} p_{\Delta t,t}(C) &\equiv \iint_{\Omega_C} dx'dx P_{\Delta t}(x|x')P_t(x') \\ &= \int d\ell\, q_{\Delta t,t}(\ell, C). \end{aligned} \tag{A15}$$

$\Sigma^{\rm trans}_{\Delta t}$ is then defined as

$$\Sigma^{\rm trans}_{\Delta t,t}(\mathcal{C}_n) \equiv k_B \sum_{C\in\mathcal{C}_n} p_{\Delta t,t-\Delta t}(C) \ln \frac{p_{\Delta t,t-\Delta t}(C)}{p_{\Delta t,t}(\tilde{C})}. \tag{A16}$$

For the stationary case, displacements that under time reversal belonged to the same class (as the bulk classes in Sec. IV A 2) canceled out and did not appear in Eq. (18). For time-dependent systems, however, the probability of belonging to a class changes with time so that also classes that do not change under time reversal (as the bulk classes) must be accounted for in Eq. (A16). From Eq. (A15) and applying the log-sum inequality to Eq. (A13) (integrating over $d\ell$ for each C), we have the bound

$$\Sigma_{\Delta t,t}(\mathcal{C}_n) \geq \Sigma^{\rm trans}_{\Delta t,t}(\mathcal{C}_n). \tag{A17}$$

b. Time-dependent driving

In cases where the forces $F(x_\tau, \lambda(\tau))$ in the Langevin dynamics have a time-dependent component λ, the time-reverse protocol [$\tilde{\lambda}(\tau) = \lambda(t-\tau)$, for a total protocol time t] must be included in the reverse path $\tilde{\mathbf{x}}$'s probabilities to define the correct pathwise entropy production

$$\Delta S_{\rm tot}(\mathbf{x}) = k_B \ln \frac{\mathcal{P}(\mathbf{x}, \lambda(\tau))}{\mathcal{P}^R(\tilde{\mathbf{x}}, \lambda(t-\tau))}. \tag{A18}$$

As in Appendix A 1 a, we consider the entropy production $\langle \Delta S_{\rm tot} \rangle^t_{t-\Delta t}$ in a time window Δt, happening between the times $t-\Delta t$ and t. Here, the propagator component of the joint probability will also have an explicit global time dependence, $P_{\Delta t,t-\Delta t}(x',x) = P_{\Delta t,t-\Delta t}(x|x')P_{t-\Delta t}(x')$, with $P_{\Delta t,t-\Delta t}(x',x)$ marking the evolution for a time Δt starting at $t-\Delta t$.

Infinitesimal time intervals. For infinitesimally small time intervals dt, the explicit time dependence of the propagator plays a secondary role and can be ignored. In order to see this, consider the entropy produced for an infinitesimal time step dt during $[t-dt, t]$, including protocol reversal from t in the next step $[t, t+dt]$,

$$dS_{\rm tot}(x|x') = k_B \ln \frac{P_{dt,t-dt}(x|x')P_{t-dt}(x')}{\tilde{P}_{dt,t}(x'|x)P_t(x)}, \tag{A19}$$

where $dS_{\rm tot}(x|x')$ denotes the entropy produced in a trajectory starting at position x' and arriving at position x. $\tilde{P}_{dt,t}(x'|x)$ is the infinitesimal propagator for the subsequent step with protocol reversal such that $\tilde{\lambda}(t+dt) = \lambda(t-dt)$. To explicitly evaluate this expression, one can make use of the explicit Gaussian expression of the propagator for infinitesimal time steps [68]:

$$P_{dt,t-dt}(x|x') \propto \exp\left[-\frac{(x-x'-v_{\bar{t}}(\bar{x})dt)^2}{4Ddt} - \frac{1}{2}\frac{\partial v_{\bar{t}}(\bar{x})}{\partial x}\right], \tag{A20}$$

where we evaluate the deterministic drift $v_\tau(x) = F(x,\lambda(\tau))/\gamma$ at the midpoint $v_{\bar{t}}(\bar{x})$, where $\bar{t} = t - dt/2$, $\bar{x} = (x' + x)/2$, and, for simplicity, assume a constant D. Denoting $dx = x - x'$, the ratio in Eq. (A19) becomes

$$\frac{dS_{\rm tot}(x|x')}{k_B} = \frac{dx}{D} v_{\bar{t}}(\bar{x}) + \ln\frac{P_{t-dt}(x')}{P_t(x)} + \mathcal{O}(dt^{3/2}), \tag{A21}$$

where we have used that the reversed protocol $\tilde{\lambda}(t+dt/2) = \lambda(t-dt/2)$. Note that evaluating the drift at the start of the protocol, $v_{t-dt}(\bar{x})$, yields the same result to leading order, because, from the Langevin equation, dx contains contributions of the order of dt and $dt^{1/2}$.

If one cannot reverse the protocol, in an infinitesimal time step, comparing the displacements starting at $t - dt$ with the ones starting at t leads to the same result as Eq. (A21), to leading order

$$\ln\frac{P_{\Delta t,t-dt}(x|x')P_{t-dt}(x')}{P_{\Delta t,t}(x'|x)P_t(x)} = \frac{dx}{D} v_t(\bar{x}) + \ln\frac{P_{t-dt}(x')}{P_t(x)} + \mathcal{O}(dt^{3/2}). \tag{A22}$$

Repeating the same steps as for the relaxation dynamics shows that the measure of irreversibility introduced in Eq. (A13) provides a lower bound to the average entropy production also for time-dependent driving, in the limit of infinitesimally small time intervals: $\Sigma_{\Delta t,t}(\mathcal{C}_n) \leq \langle \Delta S_{\rm tot}\rangle^t_{t-\Delta t}$ as $\Delta t \to 0$. For larger time intervals, the bound is not valid. This becomes more evident for faster dynamics, such as the fast pulling rates, which feature a strong time dependence of v. In Fig. 3(c), we observed a slight overestimation of the true entropy production for the faster pulling rates measured with $\Delta t = 5$ ms for the low barrier case. Note that, if one can reverse the protocol in the $q_{\Delta t,t}(-\ell,\tilde{C})$ displacements of Eq. (A13), the bound will hold for any Δt, but this is typically not operationally accessible.

APPENDIX B: FLUCTUATION THEOREM

As discussed in Appendix A, in the limit of vanishing Δt, Eq. (A1) is an equality. It then follows that

$$\frac{P_{\Delta t}(x|x')P(x')}{P_{\Delta t}(x'|x)P(x)} = e^{\Delta S_{\rm tot}(x|x')/k_B} = e^{-\Delta S_{\rm tot}(x'|x)/k_B}, \tag{B1}$$

where $\Delta S_{\rm tot}(x|x')$ denotes the entropy produced in a trajectory starting at position x' and arriving at position x. (In addition to infinitesimally short trajectories, the entropy produced is a function of the initial and final point only, also for one-dimensional trajectories as shown in Sec. I in Supplemental Material [67].) This allows us to rewrite the probability of a displacement in terms of that of its time reversal and the entropy produced along such displacement. We can rewrite Eq. (8) as

$$\begin{aligned} q_{\Delta t}(\ell,C) &\equiv \iint_{\Omega_C} dx'dx\delta(\ell-(x-x'))P_{\Delta t}(x|x')P(x') \\ &= \iint_{\Omega_C} dx'dx\delta(\ell-(x-x')) \\ &\quad\times P_{\Delta t}(x'|x)P(x)e^{-\Delta S_{\rm tot}(x'|x)/k_B}. \end{aligned} \tag{B2}$$

Exchanging the role of the starting and final position $x \leftrightarrow x'$ maps the integration domain Ω_C on to the one of its corresponding time-reversed class $\Omega_{\tilde{C}}$, so that we have

$$\begin{aligned} q_{\Delta t}(\ell,C) &= \iint_{\Omega_{\tilde{C}}} dx'dx\delta(\ell+(x-x')) \\ &\quad\times P_{\Delta t}(x|x')P(x')e^{-\Delta S_{\rm tot}(x|x')/k_B}. \end{aligned} \tag{B3}$$

Taking the ratio of this probability with the probability of a time-reversed displacement, we obtain

$$\frac{q_{\Delta t}(\ell,C)}{q_{\Delta t}(-\ell,\tilde{C})} = \langle e^{-\Delta S_{\rm tot}/k_B}|-\ell,\tilde{C}\rangle, \tag{B4}$$

which is the conditional average of the exponential of minus the entropy that is produced in a displacement, with the conditioning on the fact that the displacement is $-\ell$ and of class $\tilde{C}$. Similarly, one has

$$\frac{q_{\Delta t}(-\ell,\tilde{C})}{q_{\Delta t}(\ell,C)} = \langle e^{-\Delta S_{\rm tot}/k_B}|\ell,C\rangle, \tag{B5}$$

which is Eq. (12) in the main text. This expression can be used to provide an alternative proof that the measure of irreversibility we have introduced provides a lower bound to entropy production [Eq. (13)]. Applying Jensen inequality for convex functions, we have that

$$\langle e^{-\Delta S_{\rm tot}/k_B}|\ell,C\rangle \geq \exp\left[\langle -\Delta S_{\rm tot}/k_B|\ell,C\rangle\right]. \tag{B6}$$

Combining this with Eq. (B5), taking the log, and changing signs, we have

$$\langle \Delta S_{\rm tot}/k_B|\ell,C\rangle \geq \ln\frac{q_{\Delta t}(\ell,C)}{q_{\Delta t}(-\ell,\tilde{C})}, \tag{B7}$$

from which Eq. (13) follows, upon multiplication by $q_{\Delta t}(\ell,C)$ and integration.

[1] L. Peliti and S. Pigolotti, *Stochastic Thermodynamics: An Introduction* (Princeton University Press, Princeton, NJ, 2021).

[2] U. Seifert, *Stochastic Thermodynamics* (Cambridge University Press, Cambridge, England, 2025).

[3] G. Lan, P. Sartori, S. Neumann, V. Sourjik, and Y. Tu, *The energy–speed–accuracy trade-off in sensory adaptation*, Nat. Phys. **8**, 422 (2012).

[4] M. Skoge, S. Naqvi, Y. Meir, and N. S. Wingreen, *Chemical sensing by nonequilibrium cooperative receptors*, Phys. Rev. Lett. **110**, 248102 (2013).

[5] P. Sartori, L. Granger, C. F. Lee, and J. M. Horowitz, *Thermodynamic costs of information processing in sensory adaptation*, PLoS Comput. Biol. **10**, e1003974 (2014).

[6] C. C. Govern and P. R. ten Wolde, *Energy dissipation and noise correlations in biochemical sensing*, Phys. Rev. Lett. **113**, 258102 (2014).

[7] S. Bo, M. Del Giudice, and A. Celani, *Thermodynamic limits to information harvesting by sensory systems*, J. Stat. Mech. (2015) P01014.

[8] P. Mehta and D. J. Schwab, *Energetic costs of cellular computation*, Proc. Natl. Acad. Sci. U.S.A. **109**, 17978 (2012).

[9] J. J. Hopfield, *Kinetic proofreading: A new mechanism for reducing errors in biosynthetic processes requiring high specificity*, Proc. Natl. Acad. Sci. U.S.A. **71**, 4135 (1974).

[10] A. Murugan, D. A. Huse, and S. Leibler, *Speed, dissipation, and error in kinetic proofreading*, Proc. Natl. Acad. Sci. U.S.A. **109**, 12034 (2012).

[11] P. Sartori and S. Pigolotti, *Kinetic versus energetic discrimination in biological copying*, Phys. Rev. Lett. **110**, 188101 (2013).

[12] T. E. Ouldridge, C. C. Govern, and P. R. ten Wolde, *Thermodynamics of computational copying in biochemical systems*, Phys. Rev. X **7**, 021004 (2017).

[13] P. Sartori and S. Pigolotti, *Thermodynamics of error correction*, Phys. Rev. X **5**, 041039 (2015).

[14] X. Yang, M. Heinemann, J. Howard, G. Huber, S. Iyer-Biswas, G. Le Treut, M. Lynch, K. L. Montooth, D. J. Needleman, S. Pigolotti *et al.*, *Physical bioenergetics: Energy fluxes, budgets, and constraints in cells*, Proc. Natl. Acad. Sci. U.S.A. **118**, e2026786118 (2021).

[15] A. I. Brown and D. A. Sivak, *Theory of nonequilibrium free energy transduction by molecular machines*, Chem. Rev. **120**, 434 (2019).

[16] P. Pietzonka, A. C. Barato, and U. Seifert, *Universal bound on the efficiency of molecular motors*, J. Stat. Mech. (2016) 124004.

[17] F. Gnesotto, F. Mura, J. Gladrow, and C. Broedersz, *Broken detailed balance and non-equilibrium dynamics in living systems: A review*, Rep. Prog. Phys. **81** (2018).

[18] A. C. Barato and U. Seifert, *Thermodynamic uncertainty relation for biomolecular processes*, Phys. Rev. Lett. **114**, 158101 (2015).

[19] T. R. Gingrich, J. M. Horowitz, N. Perunov, and J. L. England, *Dissipation bounds all steady-state current fluctuations*, Phys. Rev. Lett. **116**, 120601 (2016).

[20] N. Ohga, S. Ito, and A. Kolchinsky, *Thermodynamic bound on the asymmetry of cross-correlations*, Phys. Rev. Lett. **131**, 077101 (2023).

[21] D. Santolin and G. Falasco, *Dissipation bounds the coherence of stochastic limit cycles*, Phys. Rev. Lett. **135**, 057101 (2025).

[22] K. Ptaszyński and M. Esposito, *Dissipation enables robust extensive scaling of multipartite correlations*, Phys. Rev. Lett. **135**, 057401 (2025).

[23] W. J. Greenleaf, M. T. Woodside, and S. M. Block, *High-resolution, single-molecule measurements of biomolecular motion*, Annu. Rev. Biophys. **36**, 171 (2007).

[24] M. C. Leake, *The physics of life: One molecule at a time*, Phil. Trans. R. Soc. B **368**, 20120248 (2013).

[25] A. S. Hansen, M. Woringer, J. B. Grimm, L. D. Lavis, R. Tjian, and X. Darzacq, *Robust model-based analysis of single-particle tracking experiments with spot-on*, eLife **7**, e33125 (2018).

[26] C. Bustamante, Y. Chemla, S. Liu, and M. Wang, *Optical tweezers in single-molecule biophysics*, Nat. Rev. Methods Primers **1** (2021).

[27] T. M. Muenker, G. Knotz, M. Krüger, and T. Betz, *Accessing activity and viscoelastic properties of artificial and living systems from passive measurement*, Nat. Mater. **23**, 1283 (2024).

[28] R. Tapia-Rojo, M. Mora, and S. Garcia-Manyes, *Single-molecule magnetic tweezers to probe the equilibrium dynamics of individual proteins at physiologically relevant forces and timescales*, Nat. Protoc. **19**, 1779 (2024).

[29] Eleanor K. R. Mackay, S. Marbach, B. Sprinkle, and A. L. Thorneywork, *The countoscope: Measuring self and collective dynamics without trajectories*, Phys. Rev. X **14**, 041016 (2024).

[30] U. Seifert, *Stochastic thermodynamics, fluctuation theorems and molecular machines*, Rep. Prog. Phys. **75**, 126001 (2012).

[31] C. Jarzynski, *Nonequilibrium equality for free energy differences*, Phys. Rev. Lett. **78**, 2690 (1997).

[32] G. E. Crooks, *Entropy production fluctuation theorem and the nonequilibrium work relation for free energy differences*, Phys. Rev. E **60**, 2721 (1999).

[33] U. Seifert, *Entropy production along a stochastic trajectory and an integral fluctuation theorem*, Phys. Rev. Lett. **95**, 040602 (2005).

[34] C. Battle, C. P. Broedersz, N. Fakhri, V. F. Geyer, J. Howard, C. F. Schmidt, and F. C. MacKintosh, *Broken detailed balance at mesoscopic scales in active biological systems*, Science **352**, 604 (2016).

[35] I. A. Martínez, G. Bisker, J. M. Horowitz, and J. M. Parrondo, *Inferring broken detailed balance in the absence of observable currents*, Nat. Commun. **10**, 3542 (2019).

[36] A. Dechant and S. I. Sasa, *Entropic bounds on currents in langevin systems*, Phys. Rev. E **97**, 062101 (2018).

[37] T. Koyuk and U. Seifert, *Thermodynamic uncertainty relation for time-dependent driving*, Phys. Rev. Lett. **125**, 260604 (2020).

[38] S. K. Manikandan, D. Gupta, and S. Krishnamurthy, *Inferring entropy production from short experiments*, Phys. Rev. Lett. **124**, 120603 (2020).

[39] T. Van Vu, V. T. Vo, and Y. Hasegawa, *Entropy production estimation with optimal current*, Phys. Rev. E **101**, 042138 (2020).

[40] E. Roldán, J. Barral, P. Martin, J. M. Parrondo, and F. Jülicher, *Quantifying entropy production in active fluctuations of the hair-cell bundle from time irreversibility and uncertainty relations*, New J. Phys. **23**, 083013 (2021).
[41] S. Otsubo, S. K. Manikandan, T. Sagawa, and S. Krishnamurthy, *Estimating time-dependent entropy production from non-equilibrium trajectories*, Commun. Phys. **5**, 11 (2022).
[42] S. Lee, D.-K. Kim, J.-M. Park, W. K. Kim, H. Park, and J. S. Lee, *Multidimensional entropic bound: Estimator of entropy production for langevin dynamics with an arbitrary time-dependent protocol*, Phys. Rev. Res. **5**, 013194 (2023).
[43] I. Di Terlizzi, M. Gironella, D. Herraez-Aguilar, T. Betz, F. Monroy, M. Baiesi, and F. Ritort, *Variance sum rule for entropy production*, Science **383**, 971 (2024).
[44] J. Degünther, J. van der Meer, and U. Seifert, *General theory for localizing the where and when of entropy production meets single-molecule experiments*, Proc. Natl. Acad. Sci. U.S.A. **121**, e2405371121 (2024).
[45] P. Singh and K. Proesmans, *Inferring entropy production from time-dependent moments*, Commun. Phys. **7**, 231 (2024).
[46] P. E. Harunari, A. Dutta, M. Polettini, and E. Roldán, *What to learn from a few visible transitions' statistics?*, Phys. Rev. X **12**, 041026 (2022).
[47] J. Van der Meer, B. Ertel, and U. Seifert, *Thermodynamic inference in partially accessible markov networks: A unifying perspective from transition-based waiting time distributions*, Phys. Rev. X **12**, 031025 (2022).
[48] C. Hyeon and W. Hwang, *Physical insight into the thermodynamic uncertainty relation using Brownian motion in tilted periodic potentials*, Phys. Rev. E **96**, 012156 (2017).
[49] T. Van Vu and Y. Hasegawa, *Thermodynamic uncertainty relations under arbitrary control protocols*, Phys. Rev. Res. **2**, 013060 (2020).
[50] C. Dieball and A. Godec, *Direct route to thermodynamic uncertainty relations and their saturation*, Phys. Rev. Lett. **130**, 087101 (2023).
[51] M. Chatzittofi, R. Golestanian, and J. Agudo-Canalejo, *Thermodynamic inference of correlations in nonequilibrium collective dynamics*, Phys. Rev. Res. **6**, L042012 (2024).
[52] I. Di Terlizzi, *Force-free kinetic inference of entropy production*, Phys. Rev. Lett. **135**, 237101 (2025).
[53] P. Pietzonka, F. Ritort, and U. Seifert, *Finite-time generalization of the thermodynamic uncertainty relation*, Phys. Rev. E **96**, 012101 (2017).
[54] E. Roldán and Juan M. R. Parrondo, *Estimating dissipation from single stationary trajectories*, Phys. Rev. Lett. **105**, 150607 (2010).
[55] J. Li, J. M. Horowitz, T. R. Gingrich, and N. Fakhri, *Quantifying dissipation using fluctuating currents*, Nat. Commun. **10**, 1666 (2019).
[56] R. Bao, N. Ohga, and S. Ito, *Measuring irreversibility by counting: A random coarse-graining framework*, arXiv:2508.11586.
[57] A. Gomez-Marin, J. M. R. Parrondo, and C. Van den Broeck, *Lower bounds on dissipation upon coarse graining*, Phys. Rev. E **78**, 011107 (2008).
[58] J. Gladrow, U. F. Keyser, R. Adhikari, and J. Kappler, *Experimental measurement of relative path probabilities and stochastic actions*, Phys. Rev. X **11**, 031022 (2021).
[59] J. Kappler and R. Adhikari, *Stochastic action for tubes: Connecting path probabilities to measurement*, Phys. Rev. Res. **2**, 023407 (2020).
[60] A. A. Hyman, C. A. Weber, and F. Jülicher, *Liquid-liquid phase separation in biology*, Annu. Rev. Cell Dev. Biol. **30**, 39 (2014).
[61] M. T. Woodside and S. M. Block, *Reconstructing folding energy landscapes by single-molecule force spectroscopy*, Annu. Rev. Biophys. **43**, 19 (2014).
[62] A. L. Thorneywork, J. Gladrow, Y. Qing, M. Rico-Pasto, F. Ritort, H. Bayley, A. B. Kolomeisky, and U. F. Keyser, *Direct detection of molecular intermediates from first-passage times*, Sci. Adv. **6**, eaaz4642 (2020).
[63] K. Sakamoto, T. Akimoto, M. Muramatsu, M. S. P. Sansom, R. Metzler, and E. Yamamoto, *Heterogeneous biological membranes regulate protein partitioning via fluctuating diffusivity*, PNAS Nexus **2**, pgad258 (2023).
[64] A. G. Cherstvy, A. V. Chechkin, and R. Metzler, *Particle invasion, survival, and non-ergodicity in 2d diffusion processes with space-dependent diffusivity*, Soft Matter **10**, 1591 (2014).
[65] D. T. McSwiggen, A. S. Hansen, S. S. Teves, H. Marie-Nelly, Y. Hao, A. B. Heckert, K. K. Umemoto, C. Dugast-Darzacq, R. Tjian, and X. Darzacq, *Evidence for DNA-mediated nuclear compartmentalization distinct from phase separation*, eLife **8**, e47098 (2019).
[66] S. Bo, L. Hubatsch, J. Bauermann, C. A. Weber, and F. Jülicher, *Stochastic dynamics of single molecules across phase boundaries*, Phys. Rev. Res. **3**, 043150 (2021).
[67] See Supplemental Material at http://link.aps.org/supplemental/10.1103/j3jk-k315, with additional mathematical derivations, supporting numerical and experimental investigations, how to practically estimate empirically the Kullback-Leibler divergences, and comparison to some existing methods in the literature. These include the additional Refs. [68–82].
[68] A. W. C. Lau and T. C. Lubensky, *State-dependent diffusion: Thermodynamic consistency and its path integral formulation*, Phys. Rev. E **76**, 011123 (2007).
[69] H. Risken and T. Frank, *The Fokker-Planck Equation: Methods of Solution and Applications*, Springer Series in Synergetics (Springer, Berlin Heidelberg, 1996).
[70] T. GrandPre, G. Teza, and W. Bialek, *Direct estimates of irreversibility from time series*, arXiv:2412.19772.
[71] F. Pérez-Cruz, *Kullback-leibler divergence estimation of continuous distributions*, *Proceedings of the 2008 IEEE International Symposium on Information Theory* (IEEE, New York, 2008), p. 1666.
[72] A. Lanza and S. Bo, *Nearest neighbours irreversibility estimator from displacement distributions*, https://github.com/bo-lab-kcl/IrreversibilityEstimator (2025).
[73] J. H. Fritz, B. Ertel, and U. Seifert, *Entropy estimation for partially accessible Markov networks based on imperfect observations: Role of finite resolution and finite statistics*, Phys. Rev. E **111**, 044106 (2025).
[74] M. T. Woodside, P. C. Anthony, W. M. Behnke-Parks, K. Larizadeh, D. Herschlag, and S. M. Block, *Direct*

measurement of the full, sequence-dependent folding landscape of a nucleic acid, Science **314**, 1001 (2006).
[75] E. Evans and K. Ritchie, *Dynamic strength of molecular adhesion bonds*, Biophys. J. **72**, 1541 (1997).
[76] G. Hummer, *From transition paths to transition states and rate coefficients*, J. Chem. Phys. **120**, 516 (2004).
[77] D. A. Foster, R. Petrosyan, A. G. Pyo, A. Hoffmann, F. Wang, and M. T. Woodside, *Probing position-dependent diffusion in folding reactions using single-molecule force spectroscopy*, Biophys. J. **114**, 1657 (2018).
[78] S. Otsubo, *Learning estimators for the entropy production*, https://github.com/tsuboshun/LearnEntropy (2020).
[79] S. Blaber and D. A. Sivak, *Optimal control in stochastic thermodynamics*, J. Phys. Comm. **7**, 033001 (2023).
[80] C. H. Bennett, *Efficient estimation of free energy differences from Monte Carlo data*, J. Comput. Phys. **22**, 245 (1976).
[81] A. Alemany, M. Ribezzi, and F. Ritort, *Recent progress in fluctuation theorems and free energy recovery*, AIP Conf. Proc. **1332**, 96 (2011).
[82] R. Tapia-Rojo, *Chapter three—construction and operation of high-resolution magnetic tape head tweezers for measuring single-protein dynamics under force*, in *Magnetic Tweezers for the Study of Protein Structure and Function*, Methods in Enzymology Vol. 694, edited by M. Ju Shon and T.-Y. Yoon (Academic Press, New York, 2024), pp. 83–107.
[83] D. Hartich and A. Godec, *Emergent memory and kinetic hysteresis in strongly driven networks*, Phys. Rev. X **11**, 041047 (2021).
[84] G. Wimsatt, A. Boyd, and J. Crutchfield, *Trajectory class fluctuation theorem*, J. Stat. Phys. **192**, 57 (2025).
[85] T. M. Cover and J. A. Thomas, *Elements of Information Theory* (John Wiley & Sons, New York, 2012).
[86] K. Blom, K. Song, E. Vouga, A. Godec, and D. E. Makarov, *Milestoning estimators of dissipation in systems observed at a coarse resolution*, Proc. Natl. Acad. Sci. U.S.A. **121**, e2318333121 (2024).
[87] M. Uhl, V. Weissmann, and U. Seifert, *Propagator for a driven Brownian particle in step potentials*, J. Phys. A **54**, 065002 (2021).
[88] K. Neupane, A. P. Manuel, and M. T. Woodside, *Protein folding trajectories can be described quantitatively by one-dimensional diffusion over measured energy landscapes*, Nat. Phys. **12**, 700 (2016).
[89] H. Kramers, *Brownian motion in a field of force and the diffusion model of chemical reactions*, Physica **7**, 284 (1940).
[90] J. A. Bonachela, H. Hinrichsen, and M. A. Muñoz, *Entropy estimates of small data sets*, J. Phys. A **41**, 202001 (2008).
[91] Q. Wang, S. R. Kulkarni, and S. Verdu, *Divergence estimation for multidimensional densities via k-nearest-neighbor distances*, IEEE Trans. Inf. Theory **55**, 2392 (2009).
[92] B. T. Goult, T. Zacharchenko, N. Bate, R. Tsang, F. Hey, A. R. Gingras, P. R. Elliott, G. C. Roberts, C. Ballestrem, D. R. Critchley *et al.*, *Riam and vinculin binding to talin are mutually exclusive and regulate adhesion assembly and turnover*, J. Biol. Chem. **288**, 8238 (2013).
[93] R. Tapia-Rojo, Álvaro Alonso-Caballero, and J. M. Fernández, *Talin folding as the tuning fork of cellular mechanotransduction*, Proc. Natl. Acad. Sci. U.S.A. **117**, 21346 (2020).
[94] R. Tapia-Rojo, A. Alonso-Caballero, C. L. Badilla, and J. M. Fernandez, *Identical sequences, different behaviors: Protein diversity captured at the single-molecule level*, Biophys. J. **123**, 814 (2024).
[95] K. Neupane, A. P. Manuel, J. Lambert, and M. T. Woodside, *Transition-path probability as a test of reaction-coordinate quality reveals dna hairpin folding is a one-dimensional diffusive process*, J. Phys. Chem. Lett. **6**, 1005 (2015).
[96] M. Esposito, *Stochastic thermodynamics under coarse graining*, Phys. Rev. E **85**, 041125 (2012).
[97] S. Bo and A. Celani, *Multiple-scale stochastic processes: Decimation, averaging and beyond*, Phys. Rep. **670**, 1 (2017).
[98] M. Manosas, A. Mossa, N. Forns, J. M. Huguet, and F. Ritort, *Dynamic force spectroscopy of DNA hairpins: II. Irreversibility and dissipation*, J. Stat. Mech. (2009) P02061.
[99] M. Ragwitz and H. Kantz, *Indispensable finite time corrections for Fokker-Planck equations from time series data*, Phys. Rev. Lett. **87**, 254501 (2001).
[100] D. S. Martin, M. B. Forstner, and J. A. Käs, *Apparent subdiffusion inherent to single particle tracking*, Biophys. J. **83**, 2109 (2002).
[101] J. Gore, F. Ritort, and C. Bustamante, *Bias and error in estimates of equilibrium free-energy differences from nonequilibrium measurements*, Proc. Natl. Acad. Sci. U.S.A. **100**, 12564 (2003).
[102] M. Palassini and F. Ritort, *Improving free-energy estimates from unidirectional work measurements: Theory and experiment*, Phys. Rev. Lett. **107**, 060601 (2011).
[103] D. Collin, F. Ritort, C. Jarzynski, S. B. Smith, I. Tinoco, and C. Bustamante, *Verification of the Crooks fluctuation theorem and recovery of RNA folding free energies*, Nature (London) **437**, 231 (2005).
[104] M. Rico-Pasto, A. Zaltron, S. J. Davis, S. Frutos, and F. Ritort, *Molten globule–like transition state of protein barnase measured with calorimetric force spectroscopy*, Proc. Natl. Acad. Sci. U.S.A. **119**, e2112382119 (2022).
[105] A. Alemany and F. Ritort, *Force-dependent folding and unfolding kinetics in DNA hairpins reveals transition-state displacements along a single pathway*, J. Phys. Chem. Lett. **8**, 895 (2017).
[106] A. Elosegui-Artola, R. Oria, Y. Chen, A. Kosmalska, C. Pérez-González, N. Castro, C. Zhu, X. Trepat, and P. Roca-Cusachs, *Mechanical regulation of a molecular clutch defines force transmission and transduction in response to matrix rigidity*, Nat. Cell Biol. **18**, 540 (2016).
[107] S. Le, M. Yu, L. Hovan, Z. Zhao, J. Ervasti, and J. Yan, *Dystrophin as a molecular shock absorber*, ACS Nano **12**, 12140 (2018).
[108] J. Alvarez and B. Hajek, *Equivalence of trans paths in ion channels*, Phys. Rev. E **73**, 046126 (2006).
[109] A. M. Berezhkovskii, G. Hummer, and S. M. Bezrukov, *Identity of distributions of direct uphill and downhill*

translocation times for particles traversing membrane channels, Phys. Rev. Lett. **97**, 020601 (2006).

[110] J. Gladrow, M. Ribezzi-Crivellari, F. Ritort, and U. F. Keyser, *Experimental evidence of symmetry breaking of transition-path times*, Nat. Commun. **10**, 55 (2019).

[111] I. Neri, *Estimating entropy production rates with first-passage processes*, J. Phys. A **55**, 304005 (2022).

[112] A. Raghu and I. Neri, *Thermodynamic bounds and symmetries in first-passage problems of fluctuating currents*, New J. Phys. **27**, 124602 (2025).